Smart Agricultural Technology 13 (2026) 101737

Contents lists available at ScienceDirect

Smart Agricultural Technology

journal homepage: www.journals.elsevier.com/smart-agricultural-technology

Simulation and verification of coupling characteristics of downwash airflow field and droplet field of agricultural unmanned aerial vehicle

Kun Chang [a,c], Shengde Chen [b,c], Meimei Wang [e], Junwei Liu [f], Ziming Zeng [f], Yubin Lan [b,c,d,*]

[a] School of Automobile and Transportation Engineering, Guangdong Polytechnic Normal University, Guangzhou, 510665, China
[b] College of Electronic Engineering (College of Artificial Intelligence), South China Agricultural University, Guangzhou, 510642, China
[c] National Center for International Collaboration Research on Precision Agricultural Aviation Pesticides Spraying Technology, Guangzhou, 510642, China
[d] Department of Biological and Agricultural Engineering, Texas A&M University, College Station, TX, 77843, USA
[e] School of Mechanical and Aviation Manufacturing Engineering, Anyang Institute of Technology, Anyang, 455099, China
[f] Department of Electrical and Electronic Engineering, The Hong Kong Polytechnic University, 999077, Hong Kong, China

ARTICLE INFO

Keywords:
Agriculture UAV
Downwash flow field
Droplet movement
CFD
PIV

ABSTRACT

Background: The downwash airflow generated by agricultural UAV rotors significantly affects droplet dispersion, thereby influencing spray performance and increasing the risk of drift. However, the coupled dynamics between rotor-induced airflow and droplet motion remain insufficiently understood.
Results: In this study, a two-phase CFD model incorporating various rotor speeds was developed and validated through particle image velocimetry (PIV) experiments, achieving fully coupled modeling of the entire pesticide spraying process of agricultural UAV. A functional relationship was established between rotor speed and droplet velocity distribution. The effects of rotor speed on droplet motion—velocity, velocity attenuation rate (K), and spatial distribution—were quantitatively analyzed. Results showed that the maximum droplet velocity occurred near the nozzle, reaching up to 20 m/s. As rotor speed increased, both droplet velocity and concentration increased significantly, while the velocity attenuation rate (K) decreased markedly. Within 1 m below the nozzle, all K values remained below 50 %. PIV measurements agreed well with CFD simulation results, with a minimum relative error of 1 %.
Conclusion: The integration of CFD and PIV methods provides a reliable framework for studying the interaction between UAV rotor downwash and droplet dynamics. The findings offer theoretical support for optimizing UAV spraying parameters and improving pesticide application efficiency, contributing to enhanced precision in aerial plant protection operations.

Abbreviations

CCD	Charge-coupled device
CFD	Computational fluid dynamics
DPM	Discrete phase model
DRW	Discrete phase walk(model)
FVM	Finite volume method
LES	Large Eddy simulation
PDPA	Phase doppler particle analyzer
PIV	Particle image velocimetry
RANS	Reynolds-averaged Navier-stokes
Re	Reynolds number
RF transmitter	Radio frequency transmitter
SIMPLE	Semi-implicit method for pressure-linked equations
SPIV	Stereoscopic particle image velocimetry
SST	Shear stress transport
UAV	Unmanned aerial vehicle
YAG	Yttrium aluminum garnet

1. Introduction

With the development of Unmanned Aerial Vehicle (UAV) technology, UAV have seen rapid adoption in agriculture in recent years. Their application have expanded far beyond initial uses in aerial photography and surveying, gradually evolving into a key tool supporting precision agriculture and smart farming management [1]. Beyond plant protection operations, UAV have been widely employed in farmland information sensing, such as monitoring crop growth, nutritional status, and

* Corresponding author at: College of Electronic Engineering (College of Artificial Intelligence), South China Agriculture University, Guangzhou 510642, China.
E-mail address: ylan@scau.edu.cn (Y. Lan).

https://doi.org/10.1016/j.atech.2025.101737
Received 5 November 2025; Received in revised form 8 December 2025; Accepted 16 December 2025
Available online 17 December 2025
2772-3755/© 2025 The Authors. Published by Elsevier B.V. This is an open access article under the CC BY-NC-ND license (http://creativecommons.org/licenses/by-nc-nd/4.0/).

pest and disease distribution using multispectral and hyperspectral sensors [2–4]. They are also used for crop phenotyping, enabling high-throughput acquisition of growth parameters such as plant height and leaf area index [5], as well as assisting in tasks such as variable-rate fertilization, seeding, and pollination [6]. These applications fully demonstrate the technical advantages of UAV platforms, including their flexibility, efficiency, and compatibility with various sensors. However, among the many agricultural UAV applications, crop spraying for plant protection remains one of the most technically complex and critically linked to both operational effectiveness and environmental impact. Agricultural UAV have become one of the key technologies for modernizing field management due to their many outstanding advantages, such as low operating altitude, no need for special landing aeras, flexibility and portability, and strong environmental adaptability [7–10]. Because of these characteristics, agricultural UAV are widely used in plant protection operations. However, the downwash airflow generated by the rotor blades directly affects the spraying conditions and droplet breakup [11]. Unlike conventional sprayers, the movement and deposition of droplets are much higher than the drift of knapsack sprayers or ground sprayers. At the same time, the rotor airflow generated by the UAV will make a large number of pesticide droplets attached to the fuselage, which not only leads to the external pollution of the UAV and damages the fuselage, but also requires more frequent cleaning and maintenance, reducing the operational efficiency [12,13]. However, there is still insufficient research on the effect of the mechanism of action between UAV spraying and downwash flow field on pesticide control efficiency.

When studying the flow characteristics of the downwash flow field, it is necessary to optimize the spraying system of agricultural UAV, so as to further improve the control efficiency of UAV spray and reduce the drift of spray droplets. During the flight of agricultural UAV, there are many factors that will affect the deposition distribution of droplets, such as wind speed, liquid characteristics, and relative positions of nozzles and crops. Wang et al. [37] conducted a study on the deposition distribution of droplets sprayed by UAV in a wind tunnel, and the results showed that wind speed, flight height, and droplet diameter were the most significant factors affecting the deposition distribution, while rotor airflow was the most significant factor affecting the deposition distribution, and the nozzle injection angle had no significant effect on the deposition distribution [14]. Kharim et al. evaluated the best operating parameters of the standard agricultural UAV spraying system available in the market, carried out field spraying experiments of spraying organic liquid fertilizer on the agricultural UAV, adopted water-sensitive paper to collect droplets, and conducted statistical analysis of the droplet deposition density. The test results showed that the droplet uniformity and deposition density are the highest when sprayed at 3L/min at 2m/s speed [15]. Some researchers improve the spraying efficiency by improving the corresponding control system. Meivel et al. improved the UAV sensor to improve the performance of the system. Arduino controller was used to effectively improve the efficient load of the UAV through lightweight materials and high-quality brushless motors. The micro-patch antenna was designed to control the payload of the RF transmitter, making it easy to carry out plant monitoring and pesticide spraying [16]. Yang et al. proposed an agriculture UAV control system based on the Pixhawk flight controller, realized the communication control of the flight controller and spray controller through a serial port, and realized the communication between the flight control system and spray system. A spray test was carried out on the self-built test platform of the UAV and spray system, and the effectiveness of the system was verified. In actual flight conditions, there are many unknown hazards, so more spray system testing is required [17]. In order to study the spraying condition of agricultural UAV in actual flight, Zhang et al. designed and developed an indoor spraying platform with X-Y direction movement and wind field to simulate the spraying condition of agricultural UAV [18].

At the same time, sprayers have a great impact on the coverage and efficiency of pesticide agriculture operations, but their atomization characteristics are also greatly affected by the downwash airflow. Therefore, Dorr et al. investigated the spray properties of nozzles by using particle image velocimetry (PIV) to measure the initial spray characteristics of a series of hydrodynamic nozzles and spray mixtures. The research results show that initial spray characteristics can vary depending on nozzle design, operating parameters, and spray formulation, and it was found that the initial droplet velocity was significantly correlated with droplet size (Dv0.5) and spray pressure [19]. In addition to conducting spray studies on nozzles, Nuyttens et al. developed a test platform and scheme for characterizing nozzles by using a Phase Doppler Particle Analyzer (PDPA) to investigate the effects of nozzle type, size, and pressure on spray droplet characteristics. A total of 32 nozzle pressure combinations were tested. The experimental results clearly show the effect of nozzle type, size, and pressure on the size and velocity of the droplets [20]. Creech et al. studied multiple variables affecting the droplet spectrum of herbicide spray, collected the droplet spectrum data of 720 combinations of spray application variables, and used a laser diffractometer to study the droplet spectrum to determine the droplet spectral characteristics of each treatment combination [21]. In addition, some relevant scholars have tried to use wind tunnel facilities to simulate natural wind fields and carry out research on droplet drift [22,23]. With the development of computer technology, there are also relevant researchers who apply machine learning technology to the research of agricultural UAV spray. Guo et al. quantitatively evaluated the nozzles of agricultural UAV by using four machine learning methods to study the XR110015VS nozzles, which proved the accuracy and efficiency of the application of machine learning methods in the evaluation of UAV nozzles and also proved the feasibility of using machine learning models to predict the size of droplets in the overlapping area of dual nozzles [24].

On the other hand, on the basis of experimental research, many scholars have also carried out a lot of simulation research on the aerodynamic characteristics of the downwash flow of the UAV. Fabrizio et al. studied the hydrodynamic interaction between the rotor and the downwash wake generated by the horizontal or vertical rod nozzles and used Computational Fluid Dynamics (CFD) to conduct numerical simulation on two multi-rotor UAV with different configurations (X6 and Y6). The optimization of the position of the arm of the UAV flight speed and the correct setting of the drug discharge rate are proposed [25]. By combining the compressible Reynolds-Averaged Navier-Stokes (RANS) equation, Shear Stress Transport (SST) k-ω equation, slip grid technology, and Semi-Implicit Method for Pressure-Linked Equations (SIMPLE) algorithm, Guo et al. established a CFD model of the downwash airflow during hovering of a quadrotor agriculture UAV and discussed the distribution of the downwash airflow in space-time dimension [26]. In order to study the general characteristics of the downwash flow distribution, Zheng et al. simulated the static wind field under the hovering state of a multi-rotor UAV and studied the space proportion occupied by ground effects and turbulence [27]. However, due to the complexity of the downwash flow structure of agricultural UAV, the research on the aerial spraying process is still very little. Many scholars have used the Lattice Boltzmann Method (LBM) to simulate the downwash flow field and droplet movement of full-size agricultural agriculture machines in order to accurately capture the development process of rotor tip vortices. The simulated instantaneous flow structure is consistent with the actual test results, which effectively verifies the reliability of the simulation method [22,28]. In order to study the relationship between the downwash flow in the agricultural UAV and the droplets, Yang et al. used ultraviolet light and ultraviolet–visible tracers to capture the distribution of droplets, including various cross sections, turbulent position and ground effect analysis [29]. Tang et al. studied the distribution of downwash airflow of multi-rotor UAV. Taking common eight-rotor agriculture UAV as the research object, they studied various wind vortices such as wake vortices, ground diffusion airflow, vortex ring, and "negative velocity channel" [30]. The downwash airflow generated by

the rotors of agricultural UAV can significantly improve the penetration of droplets, which indicates that the downwash airflow can effectively help the droplets to settle inside the tree crown or on the lower surface of the leaves. By using the CFD method, Zhang et al. established a prediction model of downwash airflow in a tree canopy defined as a porous medium and adopted a wireless simulation parameter measurement system to provide data verification for the numerical simulation. The results show that the airflow velocity in tree canopy is comprehensively affected by 5 factors (Load, Operation height, Canopy diameter, Tree height, Canopy density) [31]. Chang et al. conducted indoor experimental validation using a plant protection UAV two-phase flow platform to investigate the characteristics of the rotor downwash airflow field of agricultural UAVs under two different numerical calculation methods—the Finite Volume Method (FVM) and the Lattice Boltzmann Method (LBM). They analyzed airflow field characteristics under different turbulence models and selected the numerical method that most accurately reflects the features of the UAV rotor downwash airflow field [32].

Although there has been much research on the spray control system and nozzle of agricultural UAV in China and internationally, the coupling relationship between the downwash field and spray behavior of agricultural UAV has been gradually reported recently. The downwash field of agricultural UAV will not only change the deposition area of droplets but also affect the distribution of droplets. The increase of downwash speed will increase the uniformity of droplet deposition. Chang et al. studied the coupling effect of the rotor speed of agricultural UAV on the downwash wind field and droplet field. The LBM was used to conduct numerical simulation of the quadrotor agricultural UAV, and PIV was used to obtain the motion state of the droplet field below the rotor. The results showed that with the increase of rotor speed, droplet speed increased significantly. LBM and PIV can effectively reveal the motion relationship between the rotor wind field and the droplet field [33]. At the same time, the installation position of the nozzle on the agricultural UAV will also affect the drift and deposition effect of droplets. When the transverse distance between the nozzle and the rotor increases, the relative deposition amount of droplets carried by the downwash airflow generated by the rotor will also increase [34,35]. Tang et al. conducted a large eddy simulation of an agricultural unmanned helicopter and its resulting spray motion. Meanwhile, in order to evaluate the accuracy of the numerical simulation, an ultrasonic anemometer array was used to measure the downwash airflow velocity under the actual hover test and forward flight conditions. The test results were comparable with the simulated instantaneous flow structure, which proved the reliability of the simulation method [28]. Shukla et al. studied the aerodynamic interaction between rotors and used Stereoscopic Particle Image Velocimetry (SPIV) to conduct aerodynamic studies on a group of side-by-side rotors during rotor separation and hovering in the Reynolds number range, identifying and discussing the basic components of multi-rotor wake and velocity profile in a plane [36]. In recent years, a number of scholars have used the model transfer method to measure the downwash airflow of UAV under the reduced model with PIV and obtained the velocity distribution under the rotor, the motion trajectory, and attenuation of the eddy current with high accuracy, which can provide certain references for the subsequent simulation research [17,28].

In summary, although many scholars have used wireless sensor networks, ultrasonic velocimeters, and tensiometers to measure the wind field characteristics of agricultural UAV, the test results are susceptible to ambient environmental conditions——such as wind speed, wind direction, atmospheric turbulence, temperature, and humidity——which often lead to uncertain test data. Therefore, some researchers use wind tunnel equipment to generate stable wind field conditions, hoping to maintain a stable external wind field through a wind tunnel to observe changes in the rotor wind field and combine laser particle size analyzer, phase doppler particle analyzer, and other optical equipment to measure changes in rotor wind field flow field [37–39], but the accuracy of the test equipment is not enough. It is not sufficient for accurate measurement of droplet motion.

In summary, although the aforementioned studies have provided a theoretical foundation for understanding the flow mechanisms of rotor downwash fields, there remains a lack of systematic research on the coupling mechanisms between downwash airflow and droplet motion. In particular, the velocity evolution, attenuation characteristics, and spatial distribution of droplets under airflow influence are still not well understood. Existing studies have primarily focused on the visualization of airflow structures, with limited exploration of droplet dynamics under gas–liquid two-phase interaction.

In view of this, the objective of this study is to reveal the coupling mechanisms between the rotor-induced airflow field and the droplet field of agricultural UAV, and to quantitatively analyze droplet velocity variation and spatial distribution under different rotor speed conditions. A combined CFD–PIV approach is employed, in which a two-phase coupling model is developed to simulate the interaction between rotor downwash and droplet transport, allowing for an in-depth investigation into how airflow disturbances affect droplet velocity attenuation and drift behavior.

Compared with existing research, the innovations of this study are mainly reflected in the following three aspects:

(1) A gas–liquid two-phase coupling analysis framework is proposed by integrating CFD simulation and PIV measurement, enabling a systematic analysis of the effects of rotor airflow on droplet behavior;

(2) A functional relationship is quantitatively established between rotor speed and droplet velocity distribution, and the evolution of the velocity attenuation rate (K) is revealed;

(3) Numerical simulation results are validated using PIV experimental data, achieving high-accuracy reconstruction of droplet motion states and providing support for the optimization of UAV spray operation parameters.

This research provides theoretical support for further understanding the spatial dynamics of droplets in UAV-based aerial spraying, and offers scientific guidance for practical engineering applications such as spray system parameter optimization, nozzle layout strategies, and rotor structure design.

2. Materials and methods

2.1. CFD numerical simulation

Since the rotor blade is the most important component of the rotor flow field of the UAV, it is very important to establish the prepared three-dimensional model. Therefore, the rotor model on the DJI T30 agricultural UAV is taken as the research object in this paper. The rotor is scanned by the hand-held 3D scanner N700 (CREAFORMINC.) in order to obtain accurate point cloud data on each scanning surface of the rotor. Geomagic Studio software (Geomagic INC.) was used to post-process the point cloud data of each scanning surface and reconstruct the three-dimensional surface model of the rotor. The resulting UAV rotor model is shown in Fig. 1a.

According to the size of the rotor blade, a suitable calculation domain is constructed in ANSYS, set to a cylinder with a diameter of 3.4 m and a height of 3.5 m. It consists of a stationary domain and a cylindrical rotating domain containing a rotor. According to the results of the previous paper [33], the downwash airflow of agricultural UAV is mainly concentrated directly below the rotor blade. Therefore, this paper increased the mesh density of the area below the rotor blade, determined the mesh parameter with reference to previous research results [24,40], and gradually increased the mesh size along the rotor blade area. The two-layer full $Y+$ option is used to provide suitable wall treatment and good numerical simulation results are obtained. At the same time, in order to ensure the meshing quality, through the ANSYS (ver. 2022 R1, ANSYS, Canons burg, PA, USA) for grid processing, with rotor origin for the whole set up field containing the cylinders on the surface of the rotor, its geometric center is located in the center of the

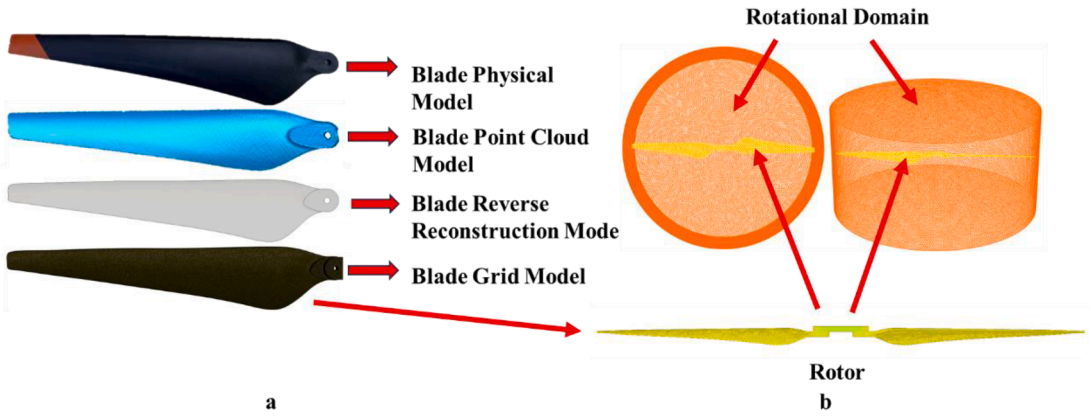


Fig. 1. a. Reverse creation of blade model; b. Rotation domain of the rotor grid.

static domain online, as shown in Fig. 1b. The geometry of the rotor brackets and nozzles is ignored because they do not significantly change the overall flow under the rotor, but add considerable computational time to the simulation. Considering that the rotor wind field is mainly around and below the blade, the BIO area is set up to further refine part of the grid area of the stationary domain in order to simulate the region of interest in the fluid domain in more detail. The number of grids in the stationary domain is 4417,891, the number of grids in the rotating domain is 115,85,060, the total number of grids in the calculation domain is 16,002,951, and the maximum skewness rate is 0.73, as shown in Fig. 2a.

Since the downwash wind field of agricultural UAV is generated by the high-speed rotation of the rotor, the SST k-ω turbulence model is selected, combined with the Lagrange tracking method of spray, and the coupling relationship between the airflow phase and the droplet phase in the region is calculated by RANS method, which is a widely used general model. The integral form of the governing equation is as follows:

$$\frac{\partial}{\partial t}\int\int\int WdV+\int\int_{\partial V} F\cdot ndS=\frac{1}{\mathrm{Re}}\int\int_{\partial V} F_v\cdot ndS$$

Where V is the control body; W is a conservation variable; **F** is the convective flux, which describes the transport of the conserved quantity due to the macroscopic motion of the fluid; S is the boundary of the control body; **n** is the normal vector outside the boundary element of the control body; **Re** is the calculated Reynolds number.

The viscous effect of the flow field is simulated by the SST k-ω turbulence model. This turbulence model combines the advantages of k-ε and k-ω turbulence models to calculate the inner and outer boundary layer, and takes into account the orthogonal divergence term, which can accurately predict the separation characteristics of the flow field, and is suitable for turbulence with a large pressure gradient and large rotation effect [41,42]. The relevant equation is as follows:

K equation:

$$\frac{D\rho k}{Dt}=\frac{\partial}{\partial x_i}\left[(\mu+\sigma_k\mu_k)\frac{\partial k}{\partial x_j}\right]+\tau_{ij}\frac{\partial u_i}{\partial x_j}-\beta^*\rho\omega$$

ω equation:

$$\frac{D\rho\omega}{Dt}=\frac{\partial}{\partial x_j}\left[(\mu+\sigma_k\mu_k)\frac{\partial\omega}{\partial x_j}\right]+\frac{\gamma}{v_t}\tau_{ij}\frac{\partial u_i}{\partial x_j}-\beta\rho\omega^2+2(1-F_1)\rho\sigma_{\omega 2}\frac{1}{\omega}\frac{\partial k}{\partial x_j}\frac{\partial\omega}{\partial x_j}$$

Where, $\tau_{ij}=-\rho\overline{u_i'u_j'}$ is the eddy viscosity coefficient; $v_t=\frac{a_1 k}{\max(a_1\omega;\Omega F_2)}$, Ω represents vorticity, and the role of the mixed function in the model is to complete the transition from the k-ω model near the wall to the k-ε model away from the wall. The rest are the default parameter values of the equation, corresponding to the k-ω model for Wilcox and the standard k-ε model, respectively.

For the boundary conditions of turbulence, the upper surface of the computational domain cylinder is set as Velocity Inlet, the lower surface as Wall, the type as a trap, the cylindrical surface as Pressure Outlet, the

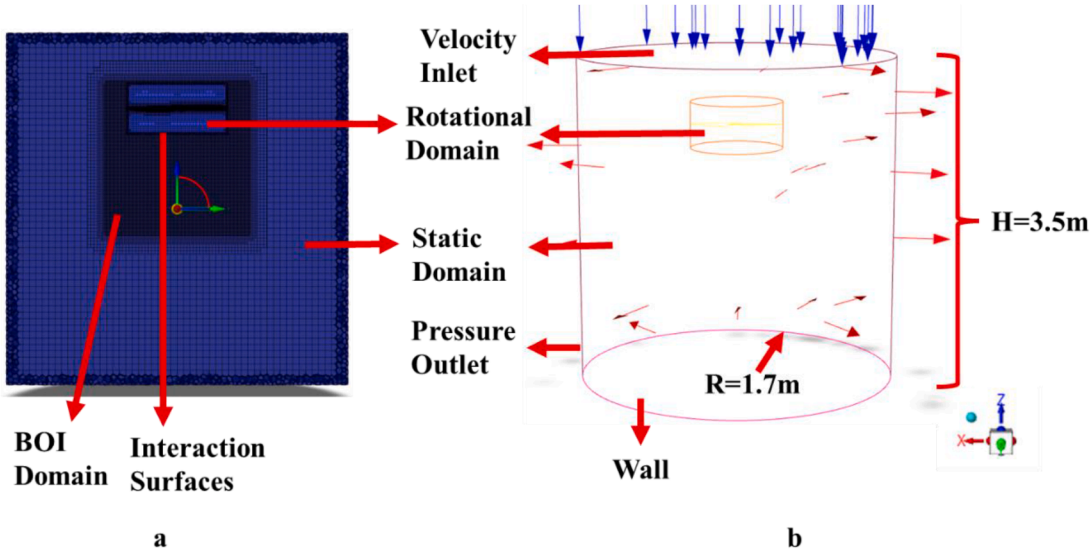


Fig. 2. a. Grid profile distribution; b. Fluid computing domain.

defined X and Y axes are perpendicular to each other, and parallel to the ground, and the Z axis is perpendicular to the ground. The acceleration of gravity along the negative Z axis is $g = 9.81 m/s^2$, as shown in Fig. 2b. The air is set to an ideal gas (ignoring the viscosity and temperature changes of the air) and the effect of the fuselage on the wind field is ignored. This method can effectively minimize the influence of the wall on the airflow, which can greatly improve the accuracy of the numerical simulation [40].

Furthermore, the Discrete Phase Model (DPM) based on the Lagrange tracking method was used to model the spray, which was used to describe the fluid motion state at different speeds (0,1500,1600,1700,1800,1900 rpm). By adding the discrete phase of the droplets into the continuous phase model of the downwash flow, the discrete phase model of the movement of the droplets is established, so as to simulate the coupling relationship between the airflow field and the droplet field. The Lagrange discrete phase model combines three factors that affect the movement of droplets (the force of the downwash flow on the droplets, the resistance in the air, and its inertia) to predict the trajectory and deposition of the droplets in the downwash flow. The motion equation of the droplet is as follows:

The definition of acceleration of droplets in the flow field:

$$\frac{du_p}{dt} = \frac{u - u_p}{\tau_p} + \frac{g(\rho_p - \rho)}{\rho_p}$$

Droplet release definition:

$$\tau_p = \frac{\rho_p d_p^2}{18\mu} \frac{24}{C_d Re}$$

Where **u** represents the airflow velocity (m/s); $\mathbf{u}_p$represents the upward droplet velocity (m/s); τ_p represents droplet release time (s); ρ indicates air density (998.2Kg/m^2); d_p denotes the diameter of the droplet; C_d represents the drag coefficient of the droplet, defined by the dynamic drag model; The relative Reynolds number **Re** is defined by the Discrete Random Walk(DRW) model.

Therefore, a virtual nozzle is used in a Discrete Phase Model (DPM) to simulate the effects of gravity and aerodynamic drag on droplet particles. The nozzle type was simulated by the flat-fan-atomizer model. A method of 'parcels' is used in which many parcels are released, each representing the same particle. To ensure good statistical accuracy, a sufficient number of Parcel must be used, so the Parcel has a Number of Streams of 200, the nozzle model is located 0.35 m directly below the center of the rotor, and the liquid particle type is inert. The nozzle parameters are determined according to the data corresponding to the nozzle used by the UAV used in the test. The steady-state and pressure-based solvers in ANSYS 2022 are used, and the discrete-phase solvers are set as unsteady solutions. The SIMPLE algorithm and the second-order upwind difference scheme were used for the discrete setting, and the number of iteration steps was 1000.

2.2. Simulation verification

The numerical simulation verification platform is mainly composed of a two-phase flow platform of agriculture UAV and PIV system and is located in the indoor environment to reduce the interference of external natural wind. The above devices and equipment were used to measure and analyze the nozzle droplet velocity under the action of the wind field of the rotor of an agricultural UAV, so as to verify the accuracy of the numerical simulation. The test site was located in the wind tunnel laboratory of the National center for International Collaboration Research on Precision Agricultural Aviation Pesticide Spraying Technology, South China Agricultural University (23°09′35.9″N113°22′19.7″ E). The average indoor ambient temperature and average relative humidity on the test day were 27 °C and 65.1 %.

2.2.1. Two-phase flow platform of agriculture UAV

The main body of the two-phase flow platform of the agriculture UAV is composed of aluminum alloy profiles, suspended under the gantry frame, and can support the use of various gestures of a variety of UAV such as quadrotor, six-rotor, and eight-rotor during testing. As shown in Fig. 3a, the quadrotor structure was adopted in this experiment, and the UAV rotor used in the experiment was fixed on the two-phase flow platform at a height of about 2 m from the ground. The parameters of the two-phase flow platform of the agriculture UAV are shown in Table 1:

The spray system of the platform is installed next to the gantry frame and is composed of a booster pump, water tank, pressure gauge, pressure-reducing valve, safety valve, relay, nozzle, and spray pipe. The spray pressure is adjusted by the pressure-reducing valve to achieve real-time nozzle spray. The nozzle used in this test is XRTEEJET11001VS, which has the same aperture as SX11001VS, the standard nozzle of T30 agriculture UAV, and is used to generate droplets with an average volume diameter of 120 μm and spray pressure of 0.4 MPa. As shown in Fig. 3b, the nozzle is installed 0.35 m below the rotor.

2.2.2. PIV system

Because the rotor vortex generated by the rotor downwash of agricultural UAV is non-periodic, the PIV system is selected as the velocity measurement device to measure the fluid domain below the rotor. PIV technology is a transient, multi-point, non-contact fluid mechanics measurement method, which can record the velocity distribution information of particles at spatial points at the same time, provide rich spatial structure and flow characteristics of the flow field, and have very high measurement accuracy. The PIV system adopted in this experiment is composed of a CCD camera (2048×2048,32fps; TSI Incorporated, USA), pulsed laser (380mJ/pulse, wavelength=532 nm; TSI Incorporated, USA), synchronizer, etc. By combining the laser generated by the laser through the optical system composed of the cylindrical mirror and the spherical mirror, the sheet light source with a beam waist thickness of about 1 mm can be produced. Adjust the frame rate according to the actual situation. The experimental arrangement of the PIV system is shown in Fig. 3a.

A 50 mm lens is used to generate a field of view large enough to capture the motion of particles in the flow field, that is, the evolution of droplets sprayed from the nozzle and scattered into the air. The Mask is set to capture the movement of droplets under different rotor speeds in the wind field. In this experiment, the pulse width of the Yttrium Aluminum Garnet (YAG) laser pulser is 3∼5 ns, the time interval of the two laser beams is 50us, the time series between the two frames of photos is 0.025 s, and the maximum distance of particle movement is less than 1 mm. Therefore, the query window is set to 36×36 pixels (a 4.6 × 4.6 mm square) to ensure that the particle move distance is less than a quarter of the length of the query window, and the overlap rate is set to 50×50 mm.

The experimental results captured by PIV are obtained from the average value of the flow field data obtained from multiple consecutive double-frame images. Based on its high sampling frequency, the turbulent kinematics energy is calculated according to the two position components of its velocity fluctuation, as follows:

$$k = \frac{1}{2}\left(u'^2 + v'^2\right)$$

Where u' is the horizontal component and v' is the vertical component.

The Insight4G software can continuously obtain AB frames of the spray image of droplets in the instantaneous state, analyze the flow field in the image, and average the flow field image to generate original data. Tecplot software is used to obtain the original data and generate the velocity vector graph. The resolution of each frame is 2048 by 2048 pixels. The nozzle is located at (150,0) in the coordinate system, and the rotor is located directly above the nozzle.

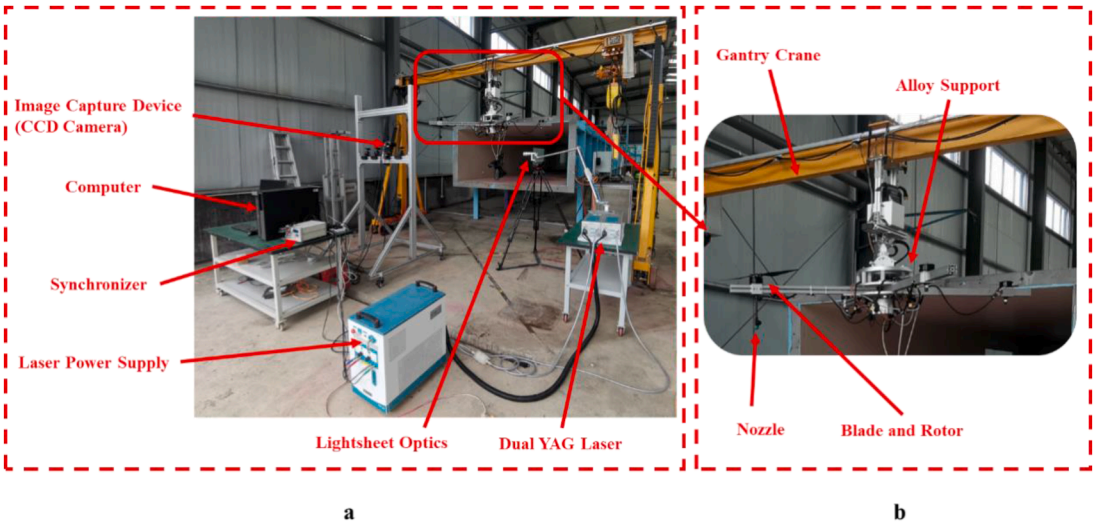


Fig. 3. a. PIV system test layout; b. Two-phase flow platform of agriculture UAV.

Table 1
Dynamic system parameters of two-phase flow platform.

Parametric	Technical Indicators
Rotor Diameter/m	1.4
Rotor Speed/rpm	0–3000
Operation Duration/min	10–15
Operating Height/m	1–3

In order to verify the accuracy of CFD simulation results, this paper designed a droplet measurement test under the coupling of the airflow field and droplet field under the rotor. As shown in Fig. 3, the droplet field directly below the nozzle is selected as the measuring range on the platform in the figure, and the corresponding rotor speed (0,1500,1600,1700,1800,1900 rpm) is selected to conduct the test. Each test is repeated three times, and the average value of the data is taken for result analysis, and the motion state of the droplet field at the nozzle below the rotor is observed during the test. The average flow characteristics and velocity distribution characteristics of droplets under the action of the wind field are analyzed.

3. Results

3.1. CFD simulation results

3.1.1. Droplet velocity distribution at different rotor speeds

As shown in Fig. 4, it is the speed distribution of the droplet field and the coupling state of the airflow field under the rotor speed of 0, 1500, 1600, 1700, 1800, and 1900 rpm respectively. Fig. 4a is the droplet field under the action of no rotor wind field, Fig. 4b is the distribution flow diagram of the droplet field under the rotor speed of 1500 rpm, and Fig. 4c is the coupling flow diagram and cloud picture of the droplet field and airflow field under the rotor speed of 1600 rpm. Fig. 4d is the flow diagram and vector diagram of the coupling of the droplet field and airflow field at 1700 rpm, Fig. 4e is the top view of the droplet field at 1800 rpm, and Fig. 4f is the volume rendering of the coupling of the droplet field and airflow field at 1900 rpm. It can be seen from Fig. 4 that the droplets sprayed from the nozzle model conform to the fan distribution state, and the velocity distribution field of the droplets under the action of the airflow field without the rotor is obviously different from that under the action of the airflow field with the rotor. It can be seen from Fig. 4a and b that the fan distribution range of the droplet velocity on the plane under the action of the airflow field without a rotor is larger than that under the action of the airflow field with the rotor. At the same time, it can be seen that under the action of the rotor flow field, the droplet velocity flow line has the phenomenon of inward contraction near the ground. As can be seen from Fig. 4c, this is due to the ground effect caused by the contact between the wind field and the ground. Under the coupling action, droplets also shrink inward due to the movement of the wind field air. By comparing the flow line of droplets under the action of the rotor flow field, it can be seen that with the increase of rotor speed, the degree of inward contraction of the droplet velocity field is greater. This shows that with the increase of rotor speed, the ground effect between the rotor flow field and the ground becomes more intense. As can be seen from Fig. 4d and e, since the simulation model is a single rotor blade of CW type, the airflow field also rotates clockwise. In addition, the droplet field is affected by the airflow, and also produces the situation of clockwise rotation. As can be seen from Fig. 4f, in the fluid domain, an obvious columnar distribution of airflow field appears below the rotor, generating an independent vortex wake. Then the diameter of the column of the lower flow field is obviously enlarged, and the turbulent wake appears. For the airflow near the ground, the ground effect leads to the diffusion of the airflow, resulting in the ground diffusion airflow, and the airflow law is similar to that in [30].

The droplet velocity field under the action of rotor flow field is further analyzed. Fig. 5 shows the scatter diagram of the coupling relationship between the droplet velocity and rotor wind speed. It can be seen from Fig. 5 that the maximum velocity of the droplet is close to 20 m/s. By comparing the velocity diagram of the droplet under the action of the rotor flow field, it can be seen that the maximum velocity of the droplet is generated by the nozzle. In combination with Fig. 5, it can be seen that the droplet velocity within 0.5 m near the nozzle is above 15 m/s. At the same time, it can be found that with the increase of rotor speed, the number of droplets with region A speed exceeding 13 m/s also presents a rising trend, and the number of droplets in region B significantly increases, while the number of droplets in region A significantly decreases. It shows that with the increase of rotor speed, the larger the downwash wind field, the movement speed of droplets also increases. By observing the distribution of droplets in region C, it can be seen that although the maximum velocity of droplets does not change basically, with the increase of rotor speed, the number of maximum velocity of droplets also moves to the right side for a lot. It shows that with the increase of rotor speed, the airflow field under the rotor is gradually enhanced, and the movement speed of the droplets is also gradually increased.

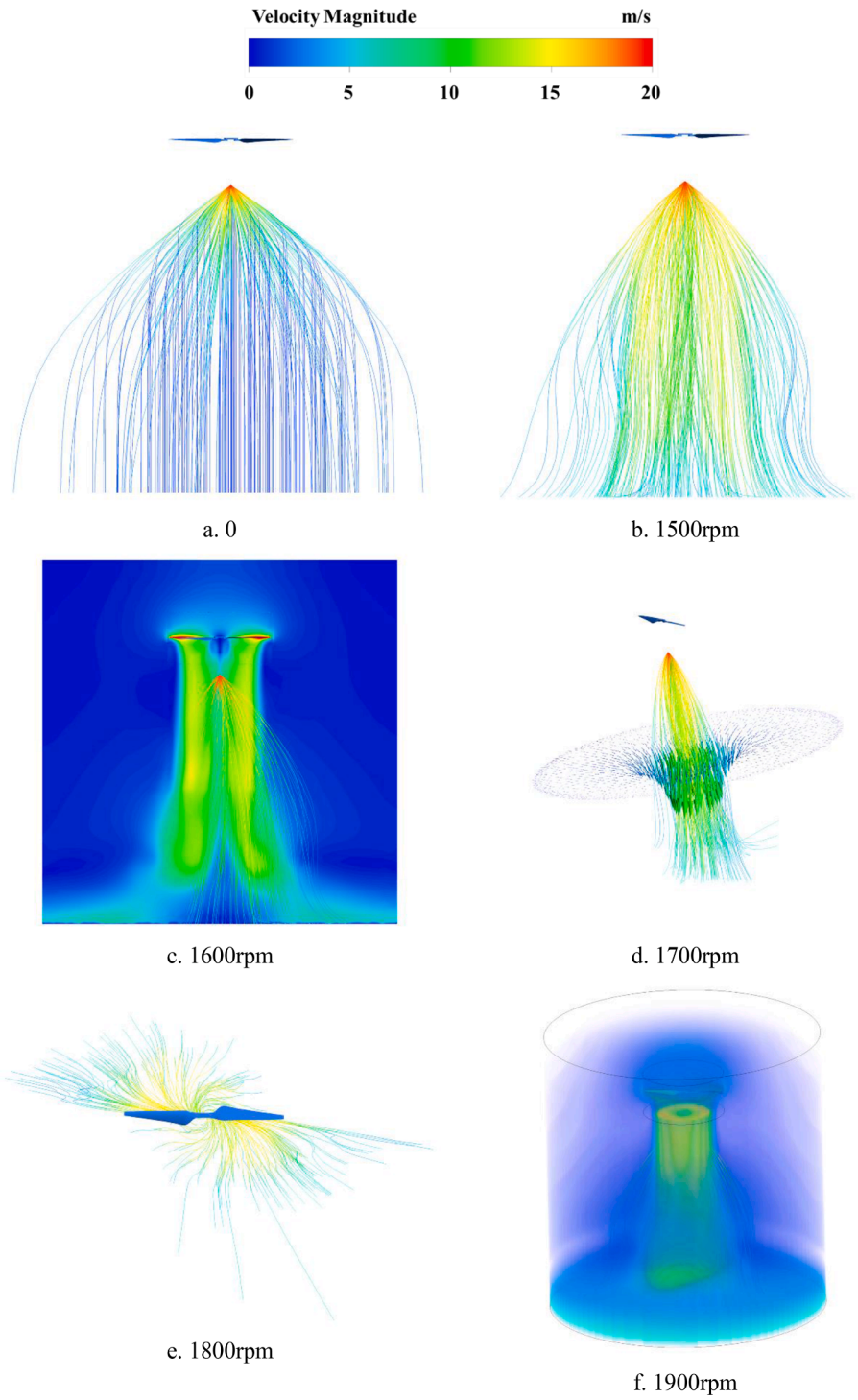


Fig. 4. Coupling diagram of flow field at different rotor speeds.

3.1.2. Droplet velocity attenuation at different rotor speeds

As shown in Fig. 6, it is the scatter diagram of the velocity distribution of the droplet velocity field at different heights of the Z-axis under the conditions of rotor speed of 0, 1500, 1600, 1700, 1800, and 1900 rpm respectively. As can be seen from Fig. 6a, under the action of a no rotor wind field, as the distance from the nozzle increases, the velocity of the droplets also decreases. The velocity distribution of droplets is mostly concentrated in region D. From Fig. 6b to f, it can be seen that the number of droplets in zone E gradually increases, while that in zone F gradually decreases. It shows that the overall droplet velocity increases with the increase in rotor speed.

In this paper, droplet velocities located 0.4, 0.45, 0.5, 0.55, 0.6, 0.65, 0.8, 1.0, 1.2, 1.4 m away from the origin in the vertical Z direction of the sprinkler head are selected, and their attenuation curves are calculated by averaging, as shown in Fig. 7a. It can be seen that the velocity attenuation of droplets increases with the distance from the sprinkler head. The closer the droplets are to the tip of the nozzle, the faster they move, far exceeding the maximum wind speed. This is because the droplets obtain the largest initial kinetic energy at the nozzle, so the droplet speed at the nozzle is the largest, and there is almost no air resistance effect. Under the action of the rotor less flow field, the velocity of the droplet decreases rapidly. When it exceeds the origin point

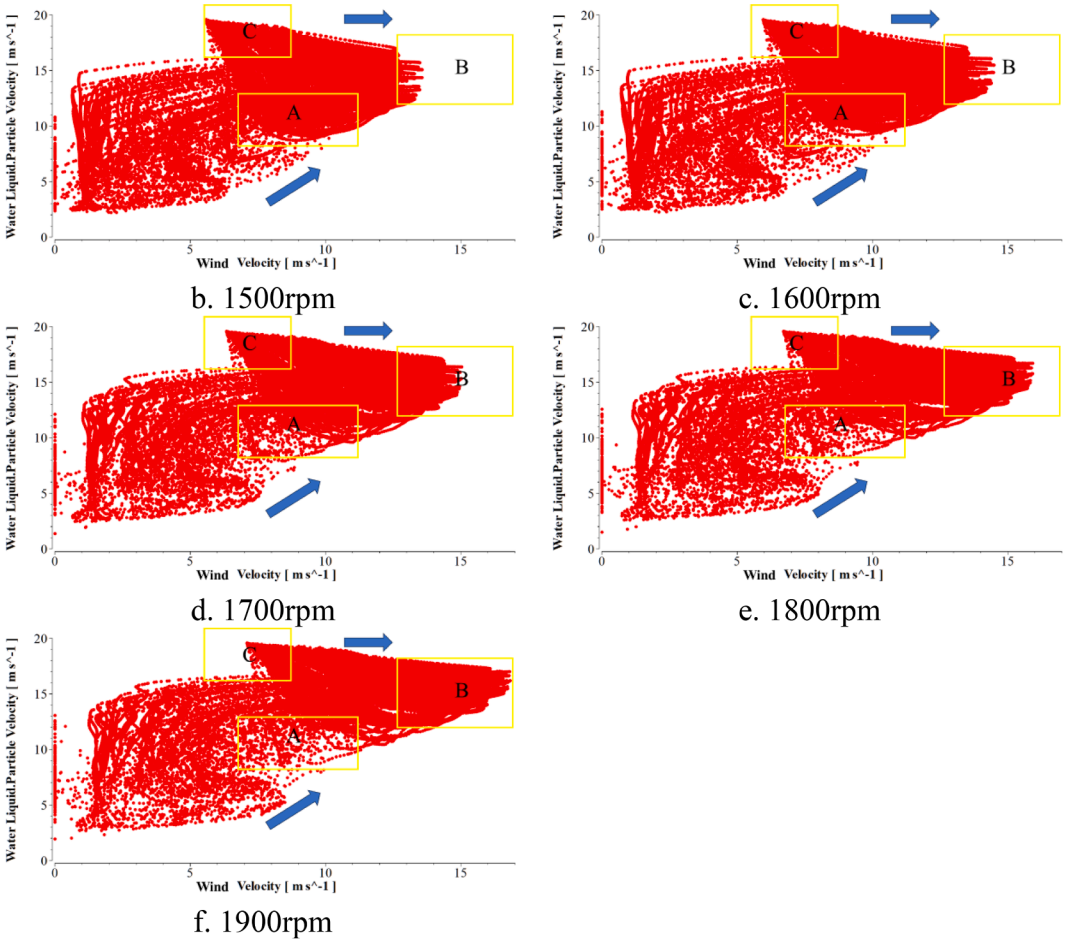


Fig. 5. Scatter diagram of droplet velocity and downwash wind speed at different rotor speeds.

by 0.6 m, the velocity of the droplet drops below 10 m/s. After 1 m from the origin, the velocity of the droplets drops below 5 m/s. Under the action of the rotor flow field, it can be seen that the velocity of the droplets does not decrease significantly. The velocity of the droplets in the origin 0.5 m is above 15 m/s, and the velocity of the droplets in the origin 1 m is above 12 m/s. It shows that the rotor downwash flow field has an obvious effect on the droplets in the droplet field, and effectively increases the velocity of the droplets. At the same time, from the change curve of the droplet velocity in the airflow field with the rotor, the droplet velocity curve experiences the change of regular-disordering-regular-disordering. This is because the initial kinetic energy of the droplets is very large after the droplets just come out of the nozzle, and the influence of the wind field is little. However, with the decrease of the kinetic energy of the droplets, the effect of the wind field on the droplets begins to gradually increase, and the attenuation of the droplets becomes irregular. However, when the rotor flow field exceeds 0.8 m, the influence of each rotor on the droplet speed is relatively regular. Then, when it exceeds the origin 1.2 m, the velocity attenuation of some droplets becomes irregular, which is because the wind field produces a ground effect after touching the ground so that the airflow near the ground then affects the droplets and disturbs the movement state of the droplets.

According to the droplet velocities at various points along the vertical Z direction from the origin, curve fitting was performed on the data using Matlab. The model of nozzle droplet velocity variation with distance in the Z direction established in this study is expressed as follows:

$$z = -12.98 - 247.9x + 0.07798y - 714.4x^2 + 0.03528xy - 909.3x^3 + 0.03908x^2y - 576.3x^4 - 0.01894x^3y - 149.x^5 - 0.0238x^4y\#$$

In this equation, z represents the droplet velocity, m/s; x represents the distance along the vertical Z direction from the nozzle, m; y represents the rotor speed, rpm.

Then, considering that the movement velocity of droplets will gradually decrease with the sedimentation distance and time, and the droplets with small particle size are particularly susceptible to the influence of external environment and drift during the sedimentation process, this paper selects the droplet movement velocity attenuation rate K as one of the indicators to measure the movement characteristics of droplets, and its calculation formula is as follows:

$$K = \frac{|V_m - V_n|}{V_n} \times 100\%$$

Where, $V_m$is the movement velocity of the droplet at the distance m from the sprinkler head, in m/s; V_n is the movement velocity of the droplet at the distance n from the nozzle, expressed in m/s.

The study combines the above analyses to statistically assess the attenuation rates of droplet velocities at selected positions. Here, n represents the droplet velocity at the nozzle (0 m), while m refers to the droplet velocities at distances of 0.4, 0.45, 0.5, 0.55, 0.6, 0.65, 0.8, 1.0, 1.2, and 1.4 m from the origin. The attenuation trend curve was obtained through calculation and is shown in the Fig. 7b. It can be seen from the figure that with the distance from the origin, the velocity attenuation rate of the droplet increases. The velocity attenuation rate K value under the action of the no rotor flow field is more than 50 % after exceeding the origin point of 0.6 m. However, under the action of the rotor flow field, the K value within 1 m of the origin is less than 40 %, and the attenuation rate changes very slowly. Further analysis of the change in velocity attenuation rate shows that the attenuation rate curve

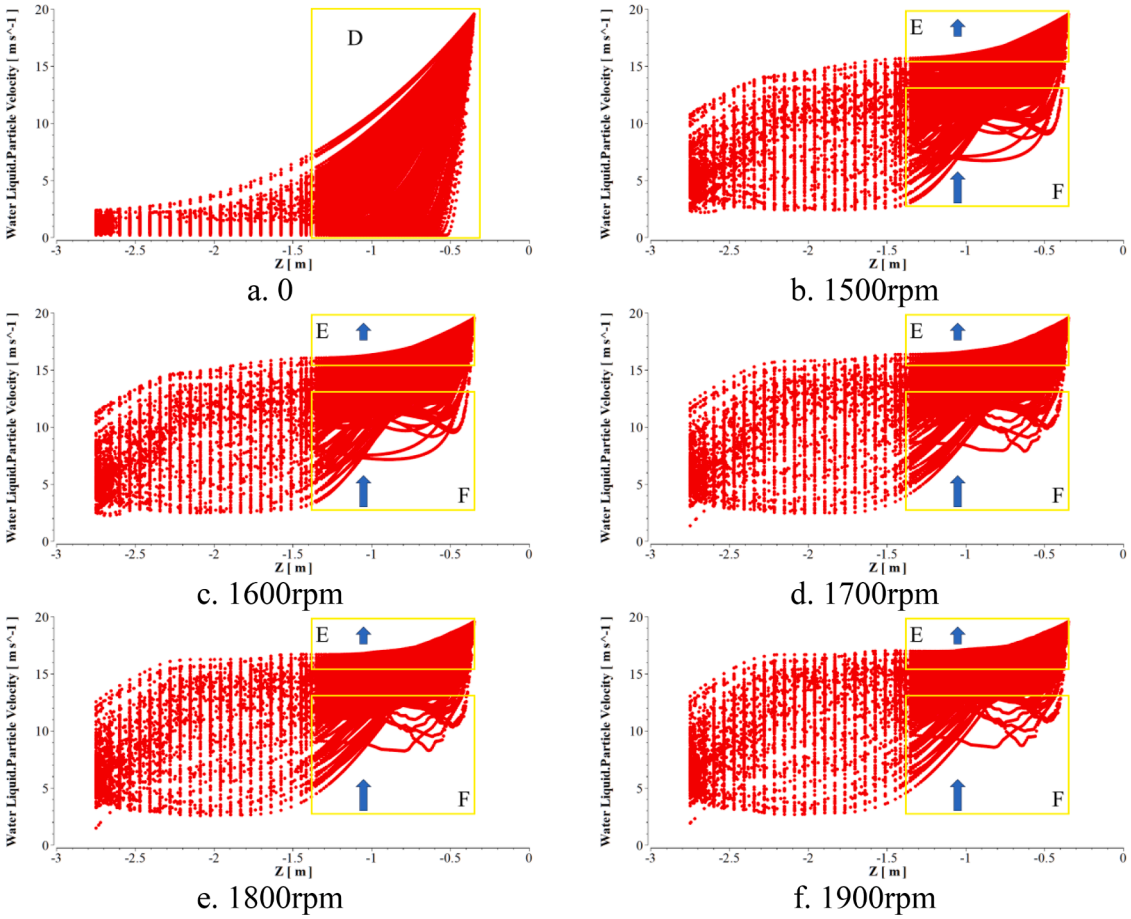


Fig. 6. Scatter diagram of droplet velocity distribution under different rotor speed and different height of Z axis.

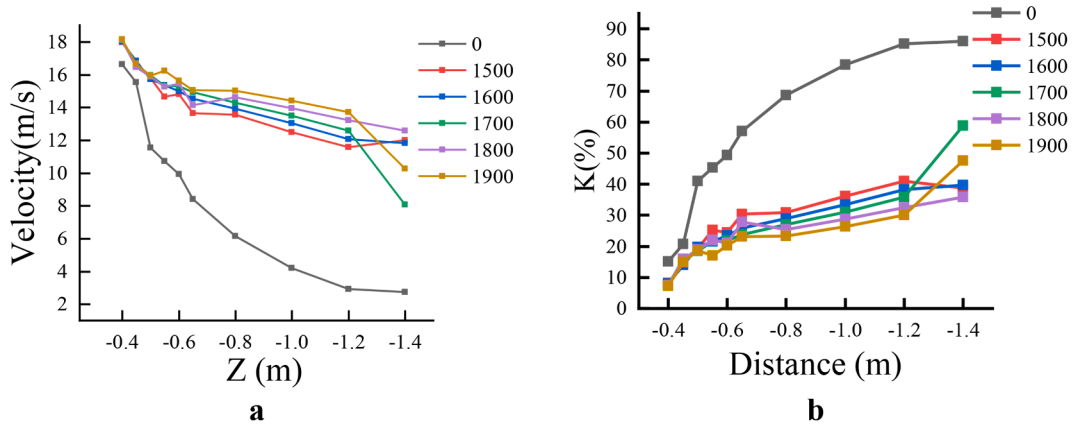


Fig. 7. a. Variation curve of droplet velocity attenuation at different altitudes and rotor speeds; b. Change curve of droplet attenuation rate at different altitudes and rotor speeds.

undergoes a pattern similar to that of the velocity curve, characterized by an alternating sequence of ordered and disordered phases. At the same time, it can be found from Figure b that as the rotor speed increases, the kinetic energy generated by the rotor flow field on droplets increases, and the droplet attenuation rate decreases.

3.1.3. Distribution of droplets quantity at different rotor speeds

As shown in Fig. 8, it is the distribution of the number of droplets velocity under the rotor speed of 0, 1500, 1600, 1700, 1800, and 1900 rpm respectively. As can be seen from Fig. 8a, under the action of no rotor wind field, the velocity of droplets is relatively concentrated in the interval less than 2 m/s, and the number of droplets in the interval less than 1 m/s is the highest, reaching 6600. In the velocity interval of 19 m/s ~ 20 m/s, the number of droplets reached 1400. In the interval of velocity less than 19 m/s, the number of droplets gradually increases with a certain law. When there is a rotor flow, the number distribution of droplets changes obviously, and the number of droplets is concentrated in the low-speed region to the medium-speed region. As can be seen from Fig. 8b, the number of droplets decreases significantly in the range with a speed less than 10m/s, while the number of droplets increases

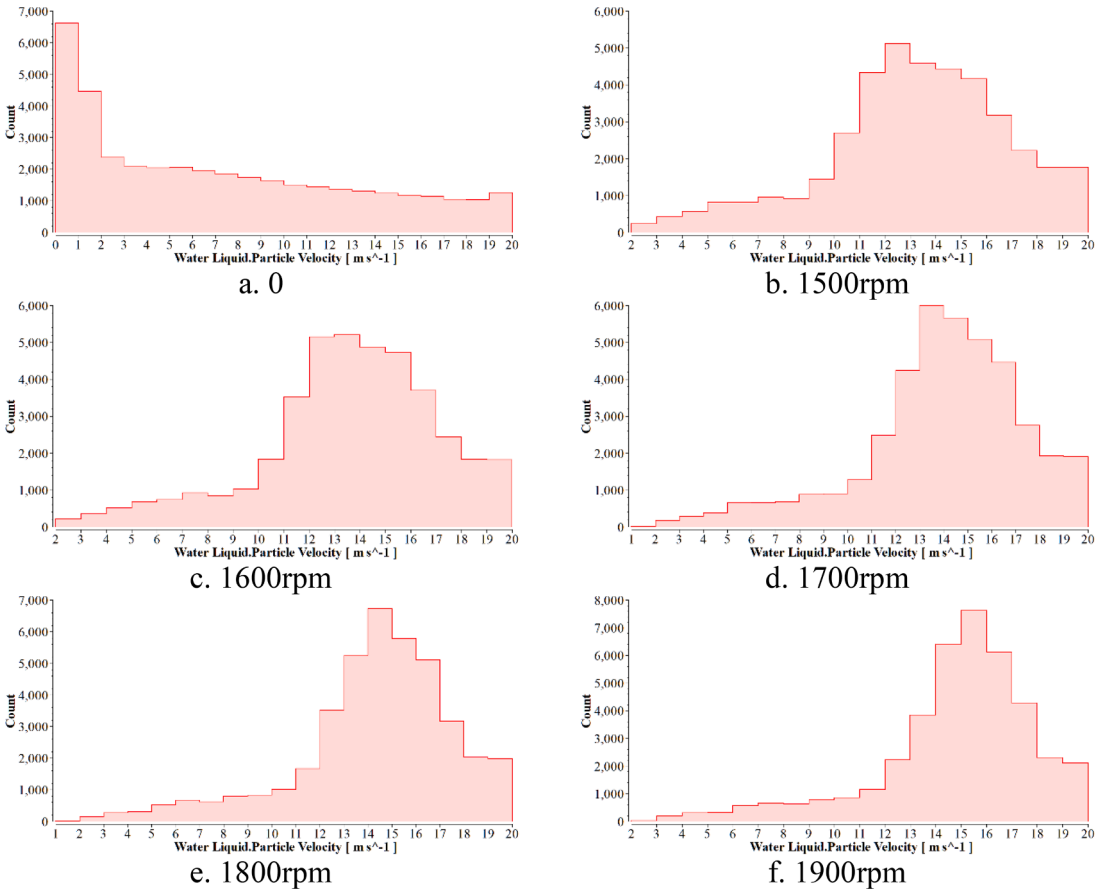


Fig. 8. Distribution of droplets velocity and quantity at different rotor speeds.

significantly in the range with a speed greater than 10m/s. In addition, it can be seen from Fig. 8b,c,d,e, and f that with the increase of rotor speed, the number of droplets increases more in the high-speed range.

According to Fig. 8b,c,d,e,f, it can be seen that under the airflow field of each rotor, the velocity ranges with the most concentrated number of droplets are 12 m/s ~ 13 m/s, 13 m/s ~ 14 m/s, 13 m/s ~ 14 m/s, 14 m/s ~ 15 m/s, and 15 m/s ~ 16 m/s respectively. The increasing number of droplets in each section shows that with the increase of rotor speed, the maximum number of droplets in the flow field is also shifting to the higher speed section. As shown in Fig. 8, within the speed range of 19 m/s ~ 20 m/s, the generation of the rotor airflow field has a certain degree of influence on the number of droplets in this area. However, with the increase of rotor speed, the enhanced airflow field has no obvious influence on the number of droplets in this area, and the number is basically kept at about 2000. Therefore, it is inferred that the rotor airflow field has no obvious effect on the velocity of droplets near the nozzle, but when the droplets leave the nozzle and are far away from the nozzle, the motion state is greatly affected by the rotor airflow field.

3.2. Verification result

3.2.1. Droplet velocity distribution at different rotor speeds

As shown in Fig. 9, it is the droplet velocity field under the rotor speed of 0, 1500, 1600, 1700, 1800, and 1900 rpm respectively. It can be seen from the figure that the spray state of droplets is mainly fan distribution, and the velocity distribution field of droplets under the action of the wind field without the rotor is obviously different from that under the action of the wind field with the rotor. In order to facilitate description, partitions are marked in the figure, and each partition represents a different speed range. The numbers are marked from 1 to 5, indicating a gradual increase in speed. The velocity of partition 1 ranges from 0 m/s to 5 m/s, partition 2 ranges from 5 m/s to 10 m/s, partition 3 ranges from 10 m/s to 15 m/s, partition 4 ranges from 15 m/s to 20 m/s, and partition 5 ranges from greater than 20 m/s. As can be seen from Fig. 9a, partition 3 is mainly concentrated in the Y direction (−100, 0), partition 2 is mainly concentrated in the Y direction (−160, 0), and partition 1 is mainly concentrated in the Y direction (−100, −150). However, under the action of the rotor wind field, different degrees of change occurred in each region, and the velocity value of droplets increased significantly. In the case of the rotor wind field, partitions 1,2 nearly disappear, and partitions 4,5 increase.

Therefore, the area of each partition is further studied. By calculating the area pixel values in each partition, the data is drawn as shown in Fig. 10. Fig. 10a represents the percentage diagram of each partition at different rotor speeds relative to the entire partition (less than 1 % is not labeled), and Fig. 10b represents the distribution diagram of the number of pixels in each partition at different rotor speeds. As can be seen from Fig. 10a, when there is no rotor speed, the droplet field in velocity partition 1 occupies the largest proportion, reaching 75.05 %, followed by velocity partition 2, accounting for 21.12 %, and velocity partition 3, accounting for 3.83 %, accounting for a relatively small proportion. Under the action of the rotor wind field, each velocity partition of the droplet velocity field changes as follows: the velocity partition 3 has the highest proportion, reaching more than 83 %, followed by the velocity partition 4, reaching more than 10 %, followed by the velocity partition 2, both above 1 %. Thus, it can be seen that the droplet velocity increases the kinetic energy of the droplet under the action of the rotor wind field, and the droplet velocity not only increases but also the proportion of the velocity range raised by the action of the wind field expands. As can be seen from Fig. 10b, the exact pixel values of each partition can be concretely seen. In the absence of a rotor wind field, the number of pixels in partition 1 reaches 294,132, that in partition 2 reaches 82,759,

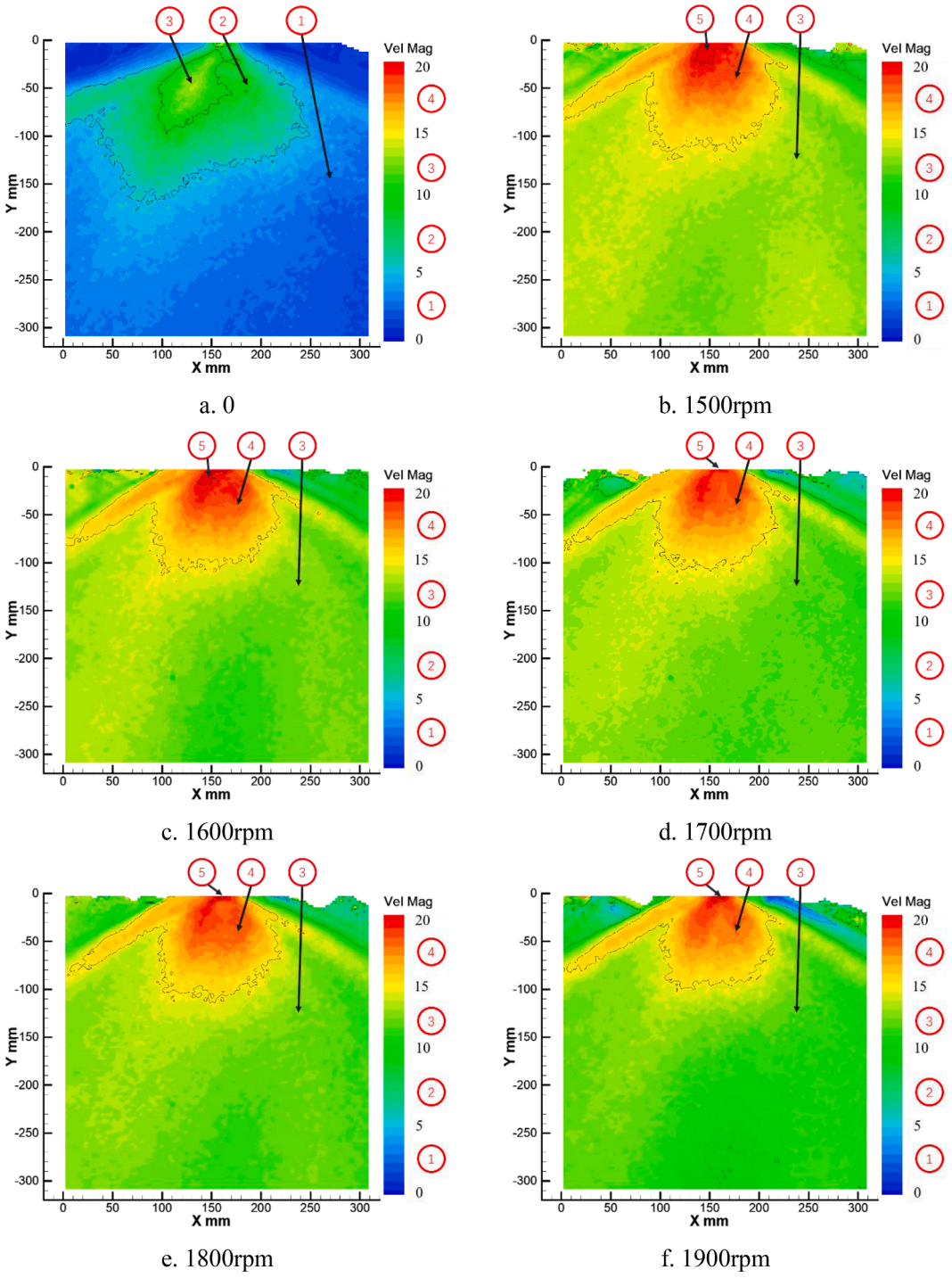


Fig. 9. Distribution of droplet velocity field at different rotor speeds.

and that in partition 3 only reaches 15,014. However, under the action of the rotor wind field, the number of partition 1 and partition 2 is quite low, and neither reaches 4000. In the speed partition 3, it exceeds 32,000, and in the speed partition 4, it exceeds 41,000. This shows that the downwash wind field of the rotor causes a huge increase in the droplet speed, especially in partition 3, where the number of pixels increases by 20 times.

The maximum droplet velocity at each rotor speed is further studied. As shown in Fig. 11a, the maximum velocity of droplets under the action of a no rotor wind field is 14.03 m/s, while that under 1500, 1600, 1700, 1800, and 1900 rpm rotor speeds is 23.61, 23.76, 27.40, 27.61 and 24.84 m/s respectively. The maximum velocity of droplets in the rotor wind field increased by 68.28 %, 69.35 %, 95.30 %, 96.79 %, and 77.05 %, respectively, compared with that without the rotor wind field. It can be seen that when the rotor speed is 1800 rpm, the maximum speed of the droplets increases the most. In the figure, V_{y-} represents the velocity component of droplets in the vertical direction. It can be seen that under the effect of the rotor wind field, the variation trend of droplets in the vertical direction is basically consistent with the variation trend of the total velocity value. The two velocity components U_{x-} and U_{x+}representing the velocity of the droplet in the horizontal direction in the figure. It can be seen that the velocity component in the vertical

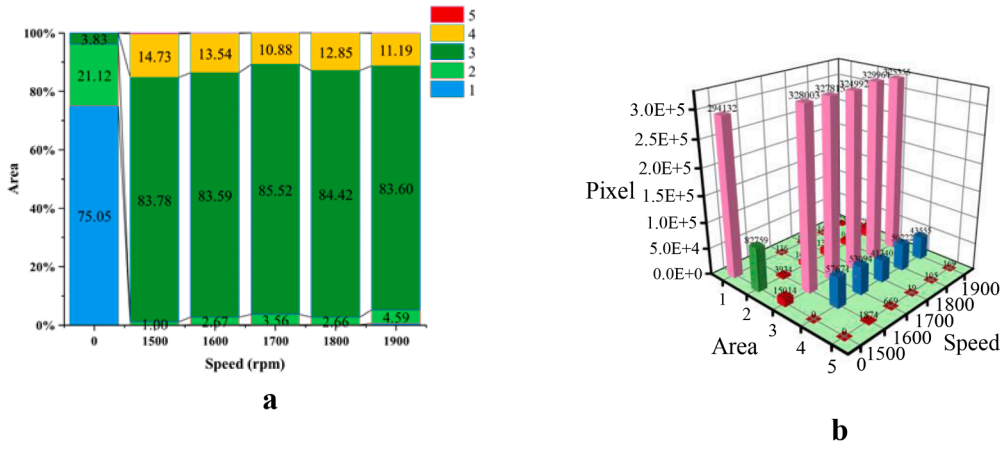


Fig. 10. a. Percentage diagram of each section relative to the whole section under different rotor speeds; b. Distribution map of the number of pixels in each interval under different rotor speeds.

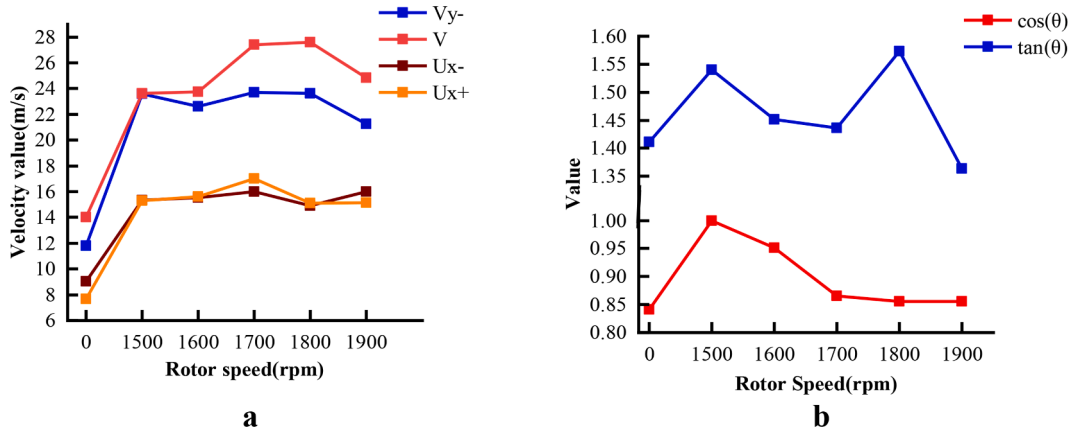


Fig. 11. a. Curve of maximum speed and velocity component at different rotor speeds; b. Velocity component change curve under different rotor speed.

direction is significantly larger than the velocity components in the horizontal direction. Comparison of the rotor wind field with the no rotor wind field shows that the rotor wind has a significant effect on the velocity in the vertical direction.

In order to further analyze the relationship between the velocity component of the droplet and the total velocity, the horizontal and vertical velocity components are further analyzed. The variation of the velocity component is expressed according to the following formula.

$$\cos(\theta) = \frac{V_y}{V}$$

$$\tan(\theta) = \frac{V_y}{V_x}$$

$\cos(\theta)$ represents the relationship between the vertical component of the velocity and the total velocity; $\tan(\theta)$ represents the relationship between the vertical and horizontal components of the velocity; θ represents the angle between the velocity vector and the horizontal direction; V indicates the maximum total speed; V_y represents the maximum vertical component of velocity; V_x represents the maximum average value of the horizontal component of the velocity.

Fig. 11b can be obtained through calculation, from which it can be seen that under the action of the rotor wind field, the $\cos(\theta)$ value increases. When the rotor speed is 1500 rpm, the $\cos(\theta)$ is the maximum, close to 1. However, with the increase of rotor speed, $\cos(\theta)$ begins to decrease gradually and gradually approaches the $\cos(\theta)$ value in the wind field without the rotor. The change trend of $\tan(\theta)$ value and $\cos(\theta)$ value is not completely consistent, showing that the first increase and then decrease, and the situation is reduced after the increase. It shows that the rotor wind field has an obvious effect on the droplet velocity, but with the increase of the rotor speed, the effect of the velocity component in the vertical direction is gradually weakened.

3.2.2. *Droplet velocity attenuation at different rotor speeds*

In order to describe the change of droplet velocity under different rotor speeds more quantitatively, origin software is used to draw the velocity value at the center position of the nozzle based on velocity vector data. Fig. 12a shows the change of droplet velocity attenuation at $X = 160$, from which it can be seen that the greater the distance from the nozzle, the greater the droplet velocity attenuation. The droplet closer to the nozzle end has the largest initial kinetic energy from the nozzle, so the droplet velocity at the nozzle is also the largest, and it is almost unaffected by air resistance. However, with the distance from the sprinkler head (greater than 150 mm), the velocity attenuation of the droplets is significantly weakened, which may be due to the fragmentation of the droplets generated by the sprinkler head, forming a smaller particle size of the droplets, and the air resistance also has a greater impact on it, so the attenuation effect is not obvious.

At the same time, in combination with the calculation method of velocity attenuation in CFD simulation results, the velocities at 0, 50, 100, 150, 200, 250, and 300 mm away from the sprinkler head are selected to measure the size of the attenuation rate, where n is the velocity of droplets at 0 of the sprinkler head, and m is 50, 100 and 300 mm away from the sprinkler head, respectively. Droplet velocity at 150, 200,

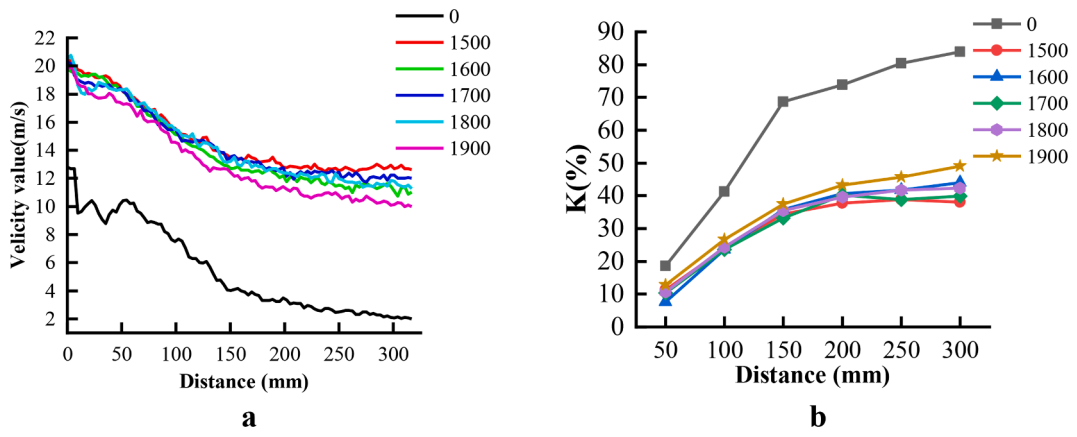


Fig. 12. a. Droplet velocity attenuation curve at $X = 160$ at different rotor speeds; b. Change curve of droplet attenuation rate at different rotor speeds.

250, 300 mm. The attenuation change curve is shown in Fig. 12b after solving and calculating. As can be seen from Fig. 12b, the greater the distance from the sprinkler, the greater the attenuation rate of the droplet motion velocity. The speed attenuation rate K value under the action of the no rotor wind field has been attenuated by 20 % at 50 mm away from the nozzle, by more than 50 % at 150 mm away from the nozzle, and by more than 80 % at 300 mm away from the nozzle. It can be seen that the droplet speed attenuation very fast. Moreover, the attenuation rate K value under the action of no rotor wind field is obviously greater than that under the action of a rotor wind field. At the distance of 150 mm from the nozzle, the droplet velocity attenuation rate K value under the action of no rotor wind field is greater than 50 %, while the K value under the action of the rotor wind field is less than 50 % within the range of 300 mm. Further analysis of the droplet velocity attenuation rate under the action of the rotor wind field shows that, on the whole, the variation trend of the velocity attenuation rate is consistent, and the K value of the attenuation rate at different rotor speeds is relatively close, indicating that the rotor speed interval of 100 rpm has little influence on the droplet velocity attenuation rate. However, it can be seen from the figure that with the increase of rotor speed, the value of velocity attenuation rate K also increases correspondingly, and the value of velocity attenuation rate K at adjacent rotational speeds is usually less than 5 %, indicating that the rotor wind field still has a certain influence on the attenuation of droplet velocity.

3.2.3. Distribution of droplets quantity at different rotor speeds

As shown in Fig. 13, it is the distribution of droplet velocity quantity under the conditions of rotor speed of 0, 1500, 1600, 1700, 1800, and 1900 rpm respectively. As can be seen from Fig. 13a, under the action of no rotor wind field, the velocity of droplets is relatively concentrated in the range of less than 5 m/s, and the number of droplets reaches the maximum in the range of 2 m/s ~ 3 m/s. The number of droplets is more than 1000, the speed range is mainly in the range of 1 m/s ~ 3.5 m/s. When there is a rotor wind field, the distribution of droplets changes obviously, and the concentration of droplets shifts from a low-speed area to a medium-speed area. It can be seen from Fig. 13b that when the rotor speed is 1500 rpm, the peak value of the number of droplets is within the range of 13 m/s ~ 13.5 m/s, which exceeds 4000.

By comparing the distribution of more than 1000 droplets in a rotor wind field, the speed ranges are 12.1 m/s to 14 m/s, 11.1 m/s to 14.2 m/s, 11.2 m/s to 13.5 m/s, 11.2 m/s to 13.6 m/s, and 10.2 m/s to 13.1 m/s. Compared with Fig. 13a, the velocity interval has changed significantly and is more concentrated in quantity. Further observation of Fig. 13c,d, e,f shows that with the increase of rotor speed, although the number of droplets is concentrated in the medium-speed region, the concentration of droplets speed begins to become relatively dispersed. In Fig. 13c and f, the number of droplets does not exceed 3000, and in Fig. 13d and e, the number of droplets does not exceed 3500. Therefore, it shows that with the increase of rotor speed, the downwash airflow field is gradually strengthened, and the movement speed of droplets is gradually increased and evenly distributed under its action, which also plays a certain role in accelerating the settlement of droplets.

4. Discussion

The downwash airflow generated by the rotor rotation of agricultural UAV will cause a change in the space flow field. This phenomenon affects the distribution and drift of the pharmaceutical solution in the process of agriculture operation of agricultural UAV. However, the current research lacks more accurate and in-depth research on the rotor downwash airflow field, which leads to more accurate and in-depth research on the spatial droplet field. This study focuses on using high-precision particle detection equipment to investigate the coupling relationship between the rotor downwash airflow field and the droplet field. By examining the flow of droplets, the study aims to explore their spatial atomization patterns, providing a basis for subsequent researchers to further study droplets and reduce pesticide waste during agricultural drone operations.

In order to verify the simulation results, the corresponding data points were compared and verified in this paper, as shown in Fig. 14.

Compare the simulated and measured values of the speed of each measurement point, and define the relative error range of the two as follows [30]:

$$e = \frac{|q_t - q_s|}{q_s}$$

Where, q_t is the droplet velocity value actually measured by PIV (m/s); q_s is the Fluent simulation speed value (m/s).

According to the above formula, Fig. 15 below shows the change curve and relative error of the average speed of the simulated and measured test at each point. It can be seen from Fig. 15 that the measured value of droplet velocity is basically smaller than the simulated value. The relative error of droplet velocity under the action of a wind field without a rotor is large. Under the action of the rotor wind field, the relative error of droplet velocity at the position of $Z = 50$ mm is very low, within 5 %. When the rotor speed is 1500 rpm, the relative error of the droplet speed is in the range of 1 % ~ 15 %. However, as the rotor speed increases, the relative error of droplet velocity becomes larger, and the maximum relative error is close to 32 %. It shows that with the increase of rotor speed, the coupling effect between the droplet field and the airflow field becomes stronger, resulting in a more complex multiphase flow phenomenon, resulting in an increasing relative error between the two. In addition, the error may also be caused by the following reasons: the parameters of the DPM model are not completely

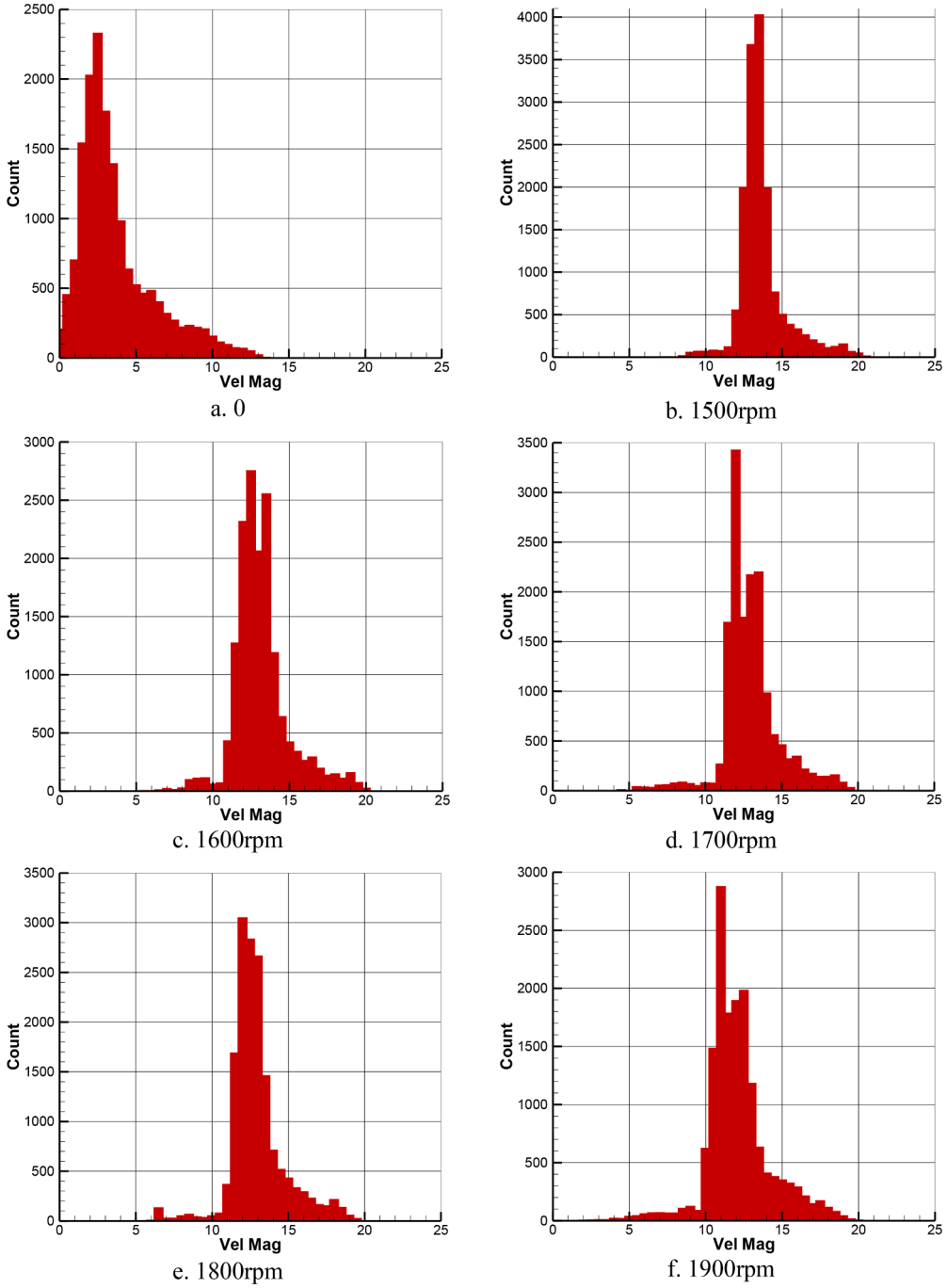


Fig. 13. Distribution of droplets velocity quantity at different rotor speeds under PIV test.

consistent with the actual parameters of the sprinkler head, and the error is further amplified during the simulation calculation, resulting in a large simulation data value; Although the indoor test can isolate most of the external influences, there will still be some wind speed interference, resulting in the actual measured value is small, affecting the measurement results.

Many of the results obtained in this paper are similar to those of previous studies. Specifically, previous studies have focused on exploring the effect of eddy current generated by downwash airflow on droplets and the variation of eddy current field with height. However, little attention has been paid to the variation characteristics of droplet velocity under the coupling relationship between the airflow field and droplet field. The change of droplet velocity will not only affect the deposition effect and distribution uniformity of droplet [22,28,40]. In addition, it will also cause changes in the particle size of the droplets and drift during the spraying operation [19]. However, there is research on the coupling of the airflow field and droplet field on droplet velocity [18]. In the past, the influence of eddy current changes on droplets was studied by numerical simulation for rotor airflow [22], while the multi-phase flow changes of droplets under the coupling of rotor airflow field (gas phase) and drop field (liquid phase) were ignored, which led to the difference in the change of spraying solution droplets. Through numerical simulation, this study explored the atomization effect of two-phase coupling of the airflow field and droplet field and proposed a reasonable pesticide spraying method considering the particle size requirements of the spray droplet. By changing the relationship between rotor speed and droplet size, different spraying requirements can be met. For example, small droplets are more likely to be absorbed by the leaf

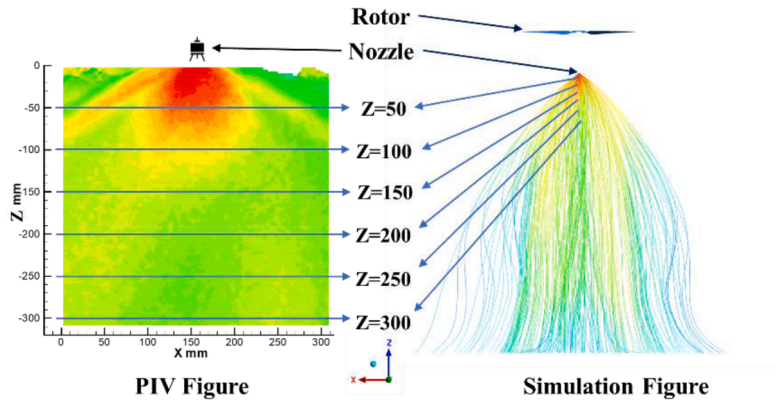


Fig. 14. Schematic diagram of droplet velocity data points.

surface of crops, or better able to penetrate the canopy of plants and kill insects (such as aphids and larvae) inside the canopy [11]. Larger droplets are more suitable for spraying herbicides for weed control over a wider area [43]. At the same time, it is also necessary to pay attention to the droplet drift in the process of agriculture, increase the downwash airflow, and control the droplet drift [9,23]. Although this study did not directly conduct drift tests, the above analysis, combined with our CFD simulations and PIV experiments, has revealed several drift-related flow phenomena—such as the outward dispersion of high-speed droplets and recirculation caused by ground effects—which are particularly pronounced under high rotor speed conditions. In future work, we plan to develop a multi-rotor coordinated wind field model to account for drift phenomena induced by complex airflow interactions during actual UAV spraying operations.

Specifically, the innovative findings derived from the above research and discussion offer practical guidance for the engineering application of agricultural UAV spraying systems in the following aspects:

(1) Optimization of rotor control strategies. Based on the observed droplet velocity attenuation patterns, a high-rotor-speed mode is recommended for dense crop canopies to enhance droplet penetration and reduce pesticide drift losses. The optimal rotor speed can be selected according to different crop types and canopy densities to effectively control droplet velocity.

(2) Nozzle co-design and configuration. Considering the vortex distribution characteristics of the airflow field, the installation position of the nozzle relative to the rotor center can be optimized to fully leverage the entrainment effect of the downwash airflow and avoid premature droplet dispersion. Future work may incorporate real-time meteorological data and UAV attitude to develop an autonomous spray control system.

(3) Decision support for precision pesticide application. By establishing a relational database linking rotor speed, droplet size, and velocity attenuation, operators can dynamically adjust spraying parameters based on pest type and crop growth stage. In addition, airflow field distribution data can support the prediction of droplet deposition areas and the optimization of nozzle layout.

However, this study still has several limitations. The research primarily focuses on the spatial flow characteristics and velocity distribution patterns of droplets under the coupling effects of the airflow field (gas phase) and droplet field (liquid phase). The main limitations are as follows:

(1) In the PIV experiments, local velocity deviations existed due to limitations in the field of view, laser intensity attenuation, and the tracking accuracy of droplet particles. Expanding the PIV measurement range to capture droplet atomization behavior in a larger spatial domain would enhance the applicability of the results to UAV-based pesticide spraying in precision agriculture.

(2) In the CFD simulations, a steady-state RANS model was used, and simplifications were made, such as neglecting secondary disturbances from the UAV fuselage and simplifying the nozzle geometry. While these choices reduced computational cost, they also resulted in a loss of flow field details. Future work will incorporate Large Eddy Simulation (LES) models or multiphase simulation approaches to improve prediction accuracy.

(3) Although the flow structure of a single rotor differs significantly from that of multi-rotor systems, this study did not consider rotor–rotor interactions or unsteady flow features. Future research will explore the turbulent characteristics of multi-rotor droplet fields and tip vortex breakdown. Additionally, the current study does not account for the interactions between droplets and crop canopies. Introducing realistic crop models would allow for the investigation of fluid–structure coupling and more accurate assessment of deposition behavior.

Although this study has revealed the interaction mechanisms between the single rotor downwash flow field and the droplet field through the coupled CFD-PIV approach, and provided a theoretical basis for optimizing the spraying parameters of agricultural UAV, several topics in this field remain worthy of in-depth exploration. Based on the finding and limitations of this study, future research could be developed in the following aspects:

(1) Complex flow field of multi-rotor systems and multiphase coupling simulation. This study focuses on a single rotor model, simplifying the complex aerodynamic interactions between rotors in actual multi-rotor UAV (such as quadrotors and hexarotors). Future research should establish full-scale multi-rotor UAV CFD models to systematically investigate the effects of interactions, merging, and dissipation processes of inter-rotor tip vortices on the overall downwash flow field structure. Special attention should be paid to the influence of rotor spacing and layout configurations on the uniformity and stability of the underlying flow field. Furthermore, more advanced transient multiphase flow simulation methods (such as combining LES with Lagrangian particle tracking) should be developed to accurately capture the effects of turbulent fluctuations on microscopic behaviors such as droplet trajectories, collisions, coalescence, and secondary atomizations.

(2) Droplet deposition research under dynamic flight conditions and real environments. This study was primarily conducted under hovering and steady-state conditions. Actual spraying operations involve dynamic maneuvers such as forward speed, climbing/descent, and turning. Future experiments and simulations should incorporate these dynamic factors to explore the coupling effects between the relative wind speed generated by UAV motion and the downwash flow field, as well as the quantitative impact on droplet deposition distribution and drift trajectories. At the same time, verification tests should be conducted in open field environments to assess the influence of environmental variables such as natural wind, temperature, humidity, and atmospheric turbulence on the “flow field-droplet-canopy” system, thereby establishing

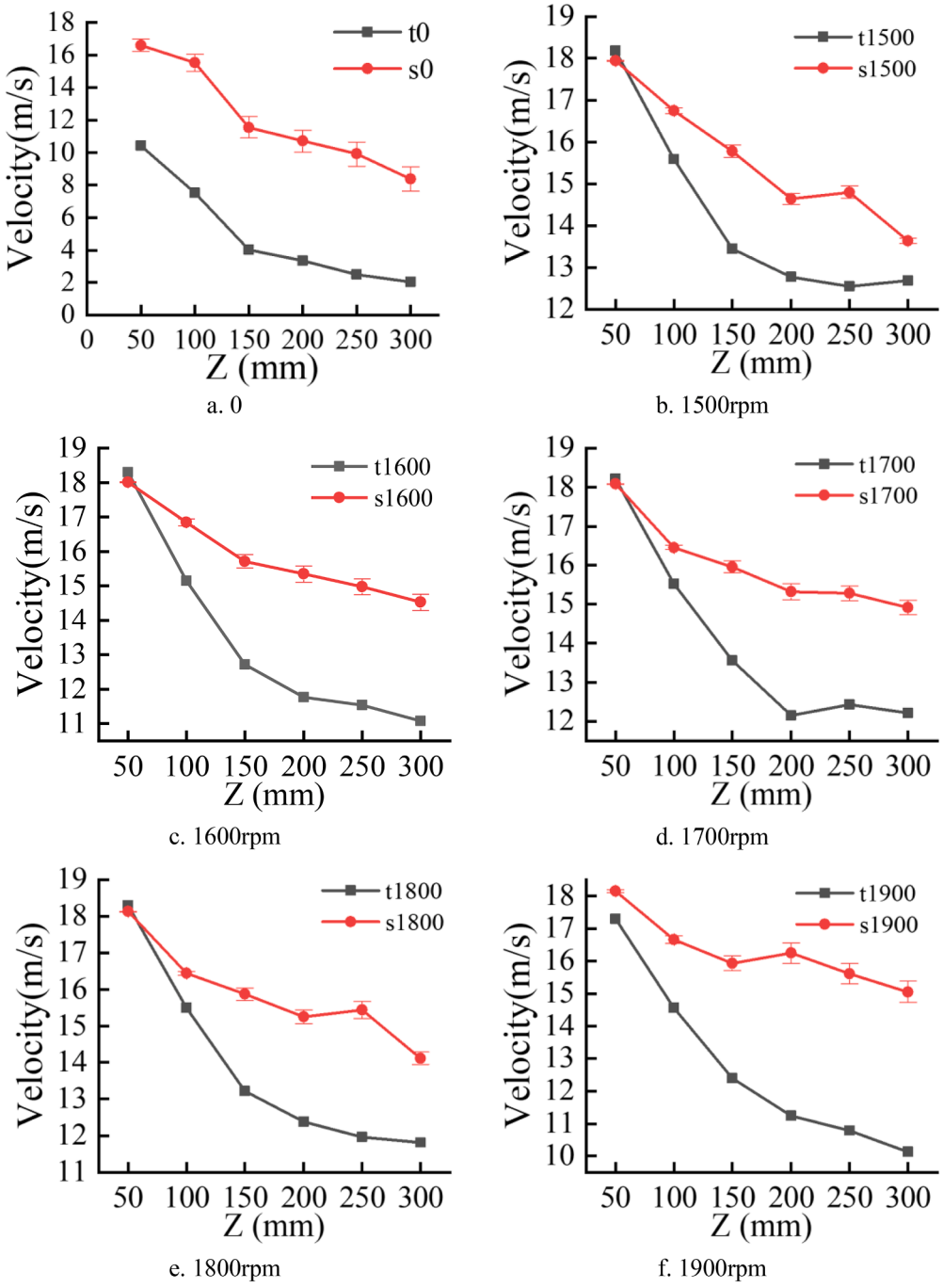


Fig. 15. Variation curve and relative error of average speed of simulated and measured test at each point.

more generalizable predictive models.

(3) Modeling of crop canopy and droplet-canopy interactions. The ultimate destination of droplets is the crop canopy. The current study has not considered the interactions between droplets and the canopy (leaves, stems). Future work should integrate realistic crop canopy structures (e.g., obtained through 3D scanning) as porous media or detailed geometric models into CFD simulations. This would involve studying the penetration and attenuation patterns of downwash airflow within the canopy, as well as the processes of droplet impact, adhesion, bounce, and runoff on leaf surface. This will provide critical theoretical support for optimizing flight altitude, speed, and spraying direction according to the canopy structural characteristics of different crops (e.g., rice, fruit trees, cotton), thereby achieving "canopy-adaptive spraying".

5. Conclusions

In order to clarify the relationship between the velocity variation of pesticide droplets under the coupling of airflow field and droplet field during the aerial spraying operation of agricultural UAV, a CFD model was established in this paper to study the spatial atomization characteristics under the coupling of downwash air droplet spraying. The accuracy of the numerical simulation is verified by capturing the droplet movement at different rotor speeds with PIV system. The main findings are as follows:

(1) The coupling relationship between droplet field and airflow field under macroscopic and local conditions is studied. The CFD model simulates the change of the droplet field under the action of the airflow field in detail under the macro conditions, and the actual test effectively

captures the change of the droplet field under the action of the airflow field under the local conditions. The coupling relationship between the two is effectively reflected from two aspects, and the velocity size, velocity attenuation, and quantity distribution of droplets under the action of the rotor downwash airflow field are summarized. A CFD–PIV coupled validation system for the downwash airflow and droplet field of agricultural UAV was established for the first time, enabling fully coupled modeling of the entire spraying process—from rotor airflow generation and droplet release to downwash influence and droplet response.

(2) The influence of rotor speed on droplet velocity, velocity decay rate (K), and spatial distribution was proposed and quantitatively analyzed, revealing the nonlinear coupling characteristics between the gas and liquid phases. The droplet descent velocity is highly correlated with the downwash airflow generated by the rotor speed. This study investigated the droplet velocity attenuation in the vertical direction of the nozzle and established a model describing the variation of droplet velocity with distance. The higher the rotor speed of the agricultural drone, the stronger the downwash airflow, leading to a greater droplet descent velocity. The maximum droplet velocity occurs near the nozzle, where the influence of the downwash airflow is relatively small. However, beyond a distance of 0.05 m from the nozzle, the droplets are significantly affected by the airflow field.

(3) The measured results can effectively verify the accuracy of CFD. The droplet velocity distribution trend is the same under the interaction between the airflow field and the droplet field, and the relative error is less than 32 %. Although the relative error of DPM model has a large value, the minimum error of simulation results can reach 1 %, which indicates that the model has a certain accuracy.

Ethical statement

This research strictly adheres to recognized academic ethical standards. We hereby declare that:

Conflicts of Interest: All authors declare that there are no known financial interests or personal relationships that could have appeared to influence the work reported in this study.

Data Authenticity and Originality: All data reported in this study are genuine and original research results. We confirm that this manuscript has not been submitted to more than one publication, and all sources of external work cited are clearly identified.

CRediT authorship contribution statement

Kun Chang: Writing – review & editing, Writing – original draft, Visualization, Validation, Methodology, Formal analysis, Conceptualization. **Shengde Chen:** Writing – review & editing, Investigation, Funding acquisition. **Meimei Wang:** Software, Resources. **Junwei Liu:** Writing – review & editing, Supervision. **Ziming Zeng:** Validation. **Yubin Lan:** Resources, Project administration, Funding acquisition.

Declaration of competing interest

The authors declare that the research was conducted in the absence of any commercial or financial relationships that could be construed as a potential conflict of interest.

Acknowledgements

The study was funded by The National Key Research and Development Plan Project (2023YFD2000200) ;The Science and Technology Planning Project of Guangzhou City, China (Grant No. 2025A04J5511); The Doctoral program construction project for research capability of Guangdong Polytechnic Normal University (Grant No. 22GPNUZDJS18); The 111 Center (D18019), The Special Fund for Science and Technology Innovation Strategy of Guangdong province (pdjh2025bc042).

Data availability

Data will be made available on request.

References

[1] S. Zhu, G. Wei, C. Longfei, C. Chen, C. Chen, Z. Qingqing, D. Suming, L. Yubin, X. Xinyu, Research status and development trends of key technologies for intelligent plant protection equipment, J. Intell. Agric. Mechaniz. 5 (2024) 1–23, https://doi.org/10.12398/j.issn.2096-7217.2024.04.001.

[2] W. Yang, W. Xu, C. Wu, B. Zhu, P. Chen, L. Zhang, Y. Lan, Cotton hail disaster classification based on drone multispectral images at the flowering and boll stage, Comput. Electron. Agr. 180 (2021) 105866, https://doi.org/10.1016/j.compag.2020.105866.

[3] H. Huang, Y. Tang, Z. Tan, J. Zhuang, C. Hou, W. Chen, J. Ren, Object-based attention mechanism for color calibration of UAV remote sensing images in precision agriculture, IEEE Trans. Geosci Remote 60 (2022) 1–13, https://doi.org/10.1109/TGRS.2022.3224580.

[4] W. Li, L. Liu, J. Li, W. Yang, Y. Guo, L. Huang, Z. Yang, J. Peng, X. Jin, Y. Lan, Spectroscopic detection of cotton Verticillium wilt by spectral feature selection and machine learning methods, Front. Plant Sci. 16 (2025) 1519001, https://doi.org/10.3389/fpls.2025.1519001.

[5] P. Zhang, Z. Zhou, H. Huang, Y. Yang, X. Hu, J. Zhuang, Y. Tang, Hybrid integrated feature fusion of handcrafted and deep features for rice blast resistance identification using UAV imagery, IEEE J.-Stars 18 (2025) 7304–7317, https://doi.org/10.1109/JSTARS.2025.3543190.

[6] S. Chen, C. Wu, L. Chen, K. Chang, S. Qian, W. Chen, Y. Lan, Design and test of aerial broadcast device for agricultural granular materials, Int. J. Precis. Agric. Avia. (2020), https://doi.org/10.33440/j.ijpaa.20200304.133.

[7] X. Xue, Y. Lan, Z. Sun, C. Chang, W.C. Hoffmann, Develop an unmanned aerial vehicle based automatic aerial spraying system, Comput. Electron. Agr. 128 (2016) 58–66, https://doi.org/10.1016/j.compag.2016.07.022.

[8] G. Wang, Y. Lan, H. Qi, P. Chen, A. Hewitt, Y. Han, Field evaluation of an unmanned aerial vehicle (UAV) sprayer: effect of spray volume on deposition and the control of pests and disease in wheat, Pest Manag. Sci. 75 (2019) 1546–1555, https://doi.org/10.1002/ps.5321.

[9] R. Zhang, L. Chen, Y. Wen, Q. Tang, L. Li, Key technologies for testing and analyzing aerial spray deposition and drift: a comprehensive review, Int. J. Precis. Agric. Aviation 3 (2020) 13–27, https://doi.org/10.33440/j.ijpaa.20200302.80.

[10] P. Chen, J.P. Douzals, Y. Lan, E. Cotteux, X. Delpuech, G. Pouxviel, Y. Zhan, Characteristics of unmanned aerial spraying systems and related spray drift: a review, Front. Plant Sci. 13 (2022), https://doi.org/10.3389/fpls.2022.870956.

[11] S. Guo, W. Yao, T. Xu, H. Ma, M. Sun, C. Chen, Y. Lan, Assessing the application of spot spray in Nanguo pear orchards: effect of nozzle type, spray volume rate and adjuvant, Pest Manag. Sci. 78 (2022) 3564–3575, https://doi.org/10.1002/ps.6999.

[12] Y. Zhan, P. Chen, W. Xu, S. Chen, Y. Han, Y. Lan, G. Wang, Influence of the downwash airflow distribution characteristics of a plant protection UAV on spray deposit distribution, Biosyst. Eng. 216 (2022) 32–45, https://doi.org/10.1016/j.biosystemseng.2022.01.016.

[13] J. Wang, C. Ma, P. Chen, W. Yao, Y. Yan, T. Zeng, S. Chen, Y. Lan, Evaluation of aerial spraying application of multi-rotor unmanned aerial vehicle for Areca catechu protection, Front. Plant Sci. 14 (2023), https://doi.org/10.3389/fpls.2023.1093912.

[14] W. Ling, C. Du, Y. Ze, N. Xindong, W. Shumao, Research on the prediction model and its influencing factors of droplet deposition area in the wind tunnel environment based on UAV spraying, IFAC-PapersOnLine 51 (2018) 274–279, https://doi.org/10.1016/j.ifacol.2018.08.174.

[15] M.N. Abd Kharim, A. Wayayok, A.R. Mohamed Shariff, A.F. Abdullah, E.M. Husin, Droplet deposition density of organic liquid fertilizer at low altitude UAV aerial spraying in rice cultivation, Comput. Electron. Agr. 167 (2019) 105045, https://doi.org/10.1016/j.compag.2019.105045.

[16] S. Meivel, K. Dinakaran, N. Gandhiraj, M. Srinivasan, Remote Sensing for UREA Spraying Agricultural (UAV) System, IEEE, 2016, pp. 1–6.

[17] S. Yang, Q. Tang, Y. Zheng, X. Liu, J. Chen, X. Li, Model migration for CFD and verification of a six-rotor UAV downwash, Int. J. Agr. Biol. Eng. 13 (2020) 10–18, https://doi.org/10.25165/j.ijabe.20201304.5569.

[18] Y. Zhang, Y. Li, Y. He, F. Liu, H. Cen, H. Fang, Near ground platform development to simulate UAV aerial spraying and its spraying test under different conditions, Comput. Electron. Agr. 148 (2018) 8–18, https://doi.org/10.1016/j.compag.2017.08.004.

[19] G.J. Dorr, A.J. Hewitt, S.W. Adkins, J. Hanan, H. Zhang, B. Noller, A comparison of initial spray characteristics produced by agricultural nozzles, Crop Prot. 53 (2013) 109–117, https://doi.org/10.1016/j.cropro.2013.06.017.

[20] D. Nuyttens, K. Baetens, M. De Schampheleire, B. Sonck, Effect of nozzle type, size and pressure on spray droplet characteristics, Biosyst. Eng. 97 (2007) 333–345, https://doi.org/10.1016/j.biosystemseng.2007.03.001.

[21] C.F. Creech, R.S. Henry, B.K. Fritz, G.R. Kruger, Influence of herbicide active ingredient, nozzle type, orifice size, spray pressure, and carrier volume rate on spray droplet size characteristics, Weed Technol. 29 (2015) 298–310, https://doi.org/10.1614/WT-D-14-00049.1.

[22] S. Wen, J. Han, Z. Ning, Y. Lan, X. Yin, J. Zhang, Y. Ge, Numerical analysis and validation of spray distributions disturbed by quad-rotor drone wake at different

flight speeds, Comput. Electron. Agr. 166 (2019) 105036, https://doi.org/10.1016/j.compag.2019.105036.
[23] G. Wang, Y. Han, X. Li, J. Andaloro, P. Chen, W.C. Hoffmann, X. Han, S. Chen, Y. Lan, Field evaluation of spray drift and environmental impact using an agricultural unmanned aerial vehicle (UAV) sprayer, Sci. Total Environ. 737 (2020) 139793, https://doi.org/10.1016/j.scitotenv.2020.139793.
[24] Q. Guo, Y. Zhu, Y. Tang, C. Hou, Y. He, J. Zhuang, Y. Zheng, S. Luo, CFD simulation and experimental verification of the spatial and temporal distributions of the downwash airflow of a quad-rotor agricultural UAV in hover, Comput. Electron. Agr. 172 (2020) 105343, https://doi.org/10.1016/j.compag.2020.105343.
[25] F. Sarghini, A. Vivo, Interference analysis of an heavy lift multirotor drone flow field and transported spraying system, Chem. Eng. Trans. (2017) 58, https://doi.org/10.3303/CET1758106.
[26] H. Guo, J. Zhou, F. Liu, Y. He, H. Huang, H. Wang, Application of machine learning method to quantitatively evaluate the droplet size and deposition distribution of the UAV spray nozzle, Appl. Sci. 10 (2020) 1759, https://doi.org/10.3390/app10051759.
[27] Y. Zheng, S. Yang, X. Liu, J. Wang, T. Norton, J. Chen, Y. Tan, The computational fluid dynamic modeling of downwash flow field for a six-rotor UAV, Front. Agric. Sci. Eng. 5 (2018) 159–167, https://doi.org/10.15302/J-FASE-2018216.
[28] Q. Tang, R. Zhang, L. Chen, W. Deng, M. Xu, G. Xu, L. Li, A. Hewitt, Numerical simulation of the downwash flow field and droplet movement from an unmanned helicopter for crop spraying, Comput. Electron. Agr. 174 (2020) 105468, https://doi.org/10.1016/j.compag.2020.105468.
[29] S. Yang, X. Liu, B. Chen, S. Li, Y. Zheng, CFD models and verification of the downwash airflow of an eight-rotor UAV, T. ASABE (2019), https://doi.org/10.13031/aim.201901018.
[30] Y. Tang, Y. Fu, Q. Guo, H. Huang, Z. Tan, S. Luo, Numerical simulation of the spatial and temporal distributions of the downwash airflow and spray field of a co-axial eight-rotor plant protection UAV in hover, Comput. Electron. Agr. 206 (2023) 107634, https://doi.org/10.1016/j.compag.2023.107634.
[31] H. Zhang, L. Qi, J. Wan, E.M. Musiu, J. Zhou, Z. Lu, P. Wang, Numerical simulation of downwash airflow distribution inside tree canopies of an apple orchard from a multirotor unmanned aerial vehicle (UAV) sprayer, Comput. Electron. Agr. 195 (2022) 106817, https://doi.org/10.1016/j.compag.2022.106817.
[32] K. Chang, S. Chen, M. Wang, J. Liao, J. Liu, Y. Lan, Numerical simulation and experimental verification of rotor airflow field based on finite volume method and lattice Boltzmann method, Drones 8 (2024) 612, https://doi.org/10.3390/drones8110612.
[33] K. Chang, S. Chen, M. Wang, X. Xue, Y. Lan, Numerical simulation and verification of rotor downwash flow field of plant protection UAV at different rotor speeds, Front. Plant Sci. (2023) 13, https://doi.org/10.3389/fpls.2022.1087636.
[34] Y. Fengbo, X. Xinyu, Z. Ling, S. Zhu, Numerical simulation and experimental verification on downwash air flow of six-rotor agricultural unmanned aerial vehicle in hover, Int. J. Agr. Biol. Eng. 40 (2017) 41–53, https://doi.org/10.25165/j.ijabe.20171004.3077.
[35] T. Qing, Z. Ruirui, C. Liping, X. Min, Y. Tongchuan, Z. Bin, Droplets movement and deposition of an eight-rotor agricultural UAV in downwash flow field, Int. J. Agr. Biol. Eng. 10 (2017) 47, https://doi.org/10.3965/j.ijabe.20171003.3075.
[36] D. Shukla, N. Komerath, Multirotor drone aerodynamic interaction investigation, Drones 2 (2018) 43, https://doi.org/10.3390/drones2040043.
[37] C. Wang, X. He, X. Wang, Z. Wang, S. Wang, L. Li, J. Bonds, A. Herbst, Z. Wang, Testing method and distribution characteristics of spatial pesticide spraying deposition quality balance for unmanned aerial vehicle, Int. J. Agr. Biol. Eng. 11 (2018) 18–26, https://doi.org/10.25165/j.ijabe.20181102.3187.
[38] Q. Tang, R. Zhang, C. Ding, L. Chen, M. Xu, G. Xu, T. Yi, Y. Wen, L. Li, W. Deng, Application of ultrasonic anemometer array to field measurements of the downwash flow of an agricultural unmanned helicopter, T. ASABE 62 (2019) 1219–1230, https://doi.org/10.13031/trans.13336.
[39] Y. Wu, L. Qi, H. Zhang, E.M. Musiu, Z. Yang, P. Wang, Design of UAV downwash airflow field detection system based on strain effect principle, Sensors 19 (2019) 2630, https://doi.org/10.3390/s19112630.
[40] Y. Zhu, Q. Guo, Y. Tang, X. Zhu, Y. He, H. Huang, S. Luo, CFD simulation and measurement of the downwash airflow of a quadrotor plant protection UAV during operation, Comput. Electron. Agr. 201 (2022) 107286, https://doi.org/10.1016/j.compag.2022.107286.
[41] F. Menter R, Improved two-equation k- turbulence models for aerodynamic flows, NASA Techn. Memorandum (1992).
[42] F. Menter R, Two-equation eddy-viscosity turbulence models for engineering applications, AIAA J. 32 (1994) 1598–1605.
[43] T.R. Butts, C.A. Samples, L.X. Franca, D.M. Dodds, D.B. Reynolds, J.W. Adams, R. K. Zollinger, K.A. Howatt, B.K. Fritz, W. Clint Hoffmann, G.R. Kruger, Spray droplet size and carrier volume effect on dicamba and glufosinate efficacy, Pest Manag. Sci. 74 (2018) 2020–2029, https://doi.org/10.1002/ps.4913.